Higher-order topology protected by latent crystalline symmetries

Lumen Eek[1], Malte Röntgen[2], Anouar Moustaj[1] and Cristiane Morais Smith[1]

1 Institute of Theoretical Physics, Utrecht University, Utrecht, 3584 CC, Netherlands
2 Laboratoire d'Acoustique de l'Université du Mans, Unite Mixte de Recherche 6613,
Centre National de la Recherche Scientifique, Avenue O. Messiaen,
F-72085 Le Mans Cedex 9, France

Abstract

We demonstrate that rotation symmetry is not a necessary requirement for the existence of fractional corner charges in C_n-symmetric higher-order topological crystalline insulators. Instead, it is sufficient to have a latent rotation symmetry, which may be revealed upon performing an isospectral reduction on the system. We introduce the concept of a filling anomaly for latent crystalline symmetric systems, and propose modified topological invariants. The notion of higher-order topology in two dimensions protected by C_n symmetry is thus generalized to a protection by latent symmetry. Our claims are corroborated by concrete examples of models that show non-trivial corner charge in the absence of C_n-symmetry. This work extends the classification of topological crystalline insulators to include latent symmetries.

Contents

1 Introduction

Topological phases of matter have been extensively studied and form a cornerstone of condensed matter physics. These phases were originally understood in the framework of the celebrated Altland-Zirnbauer classification for non-interacting systems [1]. It considers the presence of time-reversal, particle-hole, and chiral symmetry to obtain 10 symmetry classes for topological insulators (TIs) and superconductors. It was also realized that there are various relationships between the classes in different dimensions, leading to what is called the ten-fold way [2]. Later, there have been various extensions that lie outside the original Altland-Zirnbauer classification. Examples are Floquet topological materials [3], disordered materials/topological Anderson insulators [4], non-Hermitian systems [5], and topological crystalline insulators (TCI's) [6], to name a few. The latter are known to host quantized electronic boundary states protected by the geometric symmetries of the crystalline system [6–9].

Of particular interest are *higher-order topological* (crystalline) *insulators* (HOTIs). While 'conventional' TIs in D dimension host states with codimension one on their $D-1$ dimensional boundary, HOTIs host boundary states with a codimension d on their $D-d$ dimensional boundary. One way of realizing HOTIs is by considering materials with quantized higher multipole moments in the bulk. Ref. [10] proposed a classification of materials with higher multipole moments as an extension of the modern theory of electric polarization [11,12]. These systems are now known to be topological and characterized in terms of *nested Wilson loops*. However, systems without a bulk multipole moment may still give rise to quantized edge or corner states. Such systems are in a so-called obstructed atomic limit, a phase with a weaker topological protection than in the conventional topological materials. This was further investigated in Refs. [13,14], where the presence of rotation symmetry leads to the definition of rotation invariants to characterize the band topology. Energy spectra with different rotation invariants cannot be deformed into each other without closing the bulk gap and are, therefore, topologically distinct. However, the protection and classification of these novel topological phases of

matter require the presence of a geometric rotation symmetry. Additionally, the emergence of these phases is independent of time-reversal, particle-hole, and chiral symmetries, making them more vulnerable since rotational symmetries are more readily disrupted compared to spectral symmetries.

Recently, a new type of symmetry, named *latent symmetry*, has been proposed [15, 16]. A latent symmetry only becomes apparent at the reduced level upon performing a suitable dimensional reduction, the so-called *isospectral reduction* (ISR) [17]. In particular, seemingly asymmetric Hamiltonians may feature latent geometric symmetries which have a strong impact on the system's eigenstates and eigenenergies [16, 18]. This connection has been used, for instance, in the design of flat-band lattices [19], and to explain "accidental degeneracies" in band structures [20]. Very recently, latent symmetries were also used to construct latent versions of the Su-Schrieffer-Heeger (SSH) model [21] and of the non-Hermitian SSH model [22].

In this work, we explore the implications of the existence of latent symmetries on the classification of topological phases. Our main result is that the presence of a geometric rotation symmetry is not a necessary constraint for obtaining the topological phases introduced in Ref. [14]. Indeed, the requirement of a rotation symmetry can be relaxed to the less stringent condition of a *latent rotation symmetry*.

The outline of this paper is the following. In Section 2, we introduce the concept of filling anomaly in the context of the SSH model. We then relate this concept to the latent SSH model, proposed in Ref. [21], discuss the ISR in more detail, and formalise the concept of latent crystalline symmetries. In Section 3, we review the topological classification of C_n-symmetric TCI's introduced in Ref. [14] and argue how the topological invariants should be modified for latent symmetries. In Section 4, the notion of primitive generators is introduced, and the generators proposed in Ref. [14] are generalized. We propose latent primitive generators that have no direct rotation symmetry, but are latently rotation symmetric. The topological behaviour of these generators is characterised in phase diagrams using topological rotation invariants. Using the generators, we construct examples of crystalline latent HOTIs in Section 5. Finally, we conclude our work in Section 7.

2 Filling anomaly by latent symmetry

Crystalline symmetries impose restrictions on the distribution of electrons in a crystal. As a consequence, it may not be possible to maintain charge neutrality everywhere in the lattice. The simplest example of a model that exhibits this behaviour is the SSH model. Its Bloch-Hamiltonian is given by

$$h_{\text{SSH}}(k) = \begin{pmatrix} 0 & v + e^{ik} \\ v + e^{-ik} & 0 \end{pmatrix}, \tag{1}$$

where the intracell hopping is denoted by v, the intercell hopping is fixed to 1, and k is the dimensionless crystal momentum (we set the lattice constant $a = 1$). The SSH model exhibits a mirror symmetry M, that is

$$M h_{\text{SSH}}(k) M^{-1} = h_{\text{SSH}}(-k), \qquad M = \begin{pmatrix} 0 & 1 \\ 1 & 0 \end{pmatrix}. \tag{2}$$

The presence of this mirror symmetry gives rise to two gapped phases, separated by a band closing at $|v| = 1$. At half filling, the system is an insulator, and for periodic boundary conditions (PBC), each unit cell hosts one electron. Overall, charge neutrality dictates that each unit cell is composed of an ion with charge $Q = |e|$. For open boundary conditions (OBC), without cutting through unit cells, the distribution of electrons depends on the phase. As a
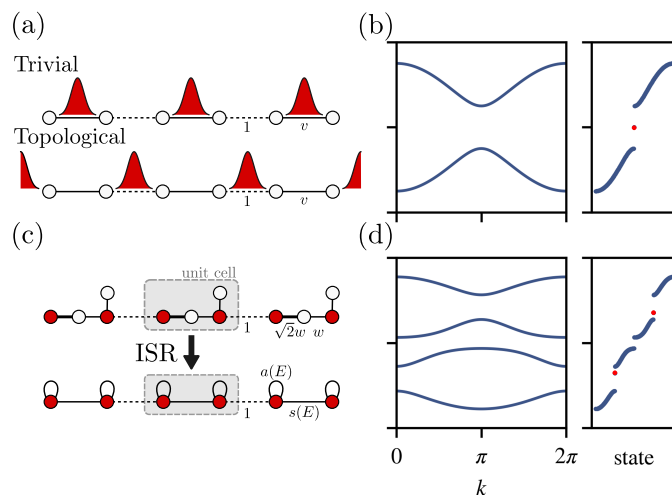
Figure 1: (a) Sketch of the SSH model in its trivial ($|v| > 1$) and topological ($|v| < 1$) phase. In the trivial (topological) phase, Wannier centers localize in the center (boundary) of the unit cell. (b) Spectrum of the SSH model for PBC (left) and OBC (right), the OBC spectrum shows in-gap edge localized modes. (c) Latent SSH model consisting of four sites with intra cell hoppings w (thin solid line) and $\sqrt{2}w$ (thick solid line). Upon performing an ISR, an energy dependent SSH model is obtained. (d) Spectrum of the latent SSH model for PBC (left) and OBC (right). The OBC spectrum shows in-gap edge states for filling 1/4 and 3/4 in the topological phase.

consequence of mirror symmetry, the Wannier centers of the electrons can only be located at either the center or the edge of a unit cell. For $|v| > 1$ (trivial phase), the Wannier centers are located at the center of the unit cell and the system can be adiabatically connected to the trivial atomic limit. On the other hand, when $|v| < 1$ (topological phase), the Wannier centers sit at the edge of the unit cell and the system can be connected to its obstructed atomic limit. The Wannier centers in both phases of the SSH model are shown in Fig. 1(a). In the trivial phase, N electrons can be distributed symmetrically over N unit cells to yield charge neutrality. However, in the topological phase, this is no longer possible. N unit cells can only be filled in a symmetric manner using $N - 1$ or $N + 1$ electrons. Since mirror symmetry requires the energies of the edge states to be degenerate [see Fig. 1(b)], increasing the Fermi energy yields an increase of $N - 1$ electrons to $N + 1$ electrons, skipping N. This leads us to the notion of a *filling anomaly* η [14], associated with a crystalline symmetry dividing the lattice in n sectors, each spanning an angle of $2\pi/n$ rad, with $n \in \mathbb{Z}$,

$$\eta = \#\text{ions} - \#\text{electrons} \qquad \mod n. \tag{3}$$

For the SSH model in the topological phase, we obtain $\eta = N - (N + 1) \mod 2 = 1$. Mirror symmetry distributes this charge imbalance over the two sides of the system, such that there will be a fractional boundary charge of $e/2$ at the ends of the system. Consequently, the dipole moment in the topological phase equals $p = e/2$, while it vanishes in the trivial phase.

2.1 Isospectral reduction and latent symmetry

Recently, Ref. [21] showed that although mirror symmetry leads to topological edge states in the SSH model, its not a necessary constraint. Indeed, the requirement of preserved mirror symmetry can be relaxed to preserved *latent* mirror symmetry. A latent symmetry is hidden and only becomes apparent upon performing what is called an isospectral reduction (ISR)—akin to an effective Hamiltonian—on the system [15]. Take a Hamiltonian H as a starting

point. The Hilbert space on which it acts may be partitioned in a set S and its complement $\overline{S}$. The ISR $\mathcal{R}_S(H, E)$ of H is then defined through

$$\mathcal{R}_S(H, E) = H_{SS} - H_{S\overline{S}}\left(H_{\overline{S}\overline{S}} - E\mathbb{I}\right)^{-1} H_{\overline{S}S}, \tag{4}$$

where $\mathbb{I}$ is the identity matrix [17]. The ISR converts the linear eigenvalue problem $H\psi = E\psi$ into a reduced, albeit non-linear, eigenvalue problem $\mathcal{R}_S(H, E)\psi_S = E\psi_S$. For example, consider the Bloch Hamiltonian

$$h_{\text{LSSH}}(k) = \begin{pmatrix} 0 & e^{ik} & \sqrt{2}w & 0 \\ e^{-ik} & 0 & w & w \\ \sqrt{2}w & w & 0 & 0 \\ 0 & w & 0 & 0 \end{pmatrix}, \tag{5}$$

which is also depicted in Fig. 1(c) for OBC. By inspection, one can conclude that this Hamiltonian does not have a mirror symmetry. Nevertheless, upon performing an ISR over the red sites, we obtain

$$\mathcal{R}_S[h_{\text{LSSH}}(k), E] = \begin{pmatrix} a(E) & s(E) + e^{ik} \\ s(E) + e^{-ik} & a(E) \end{pmatrix} \equiv \mathfrak{h}_{\text{LSSH}}(k), \tag{6}$$

which bears a strong resemblance with the SSH model given in Eq. (1), though with energy-dependent on-site potential $a(E) = 2w^2/E$ and coupling $s(E) = \sqrt{2}w^2/E$. At the level of the ISR, there is a mirror symmetry: $M\mathfrak{h}_{\text{LSSH}}(k)M^{-1} = \mathfrak{h}_{\text{LSSH}}(-k)$.[1] In other words, the system given by Eq. (5) hosts a *latent mirror symmetry*, which is revealed through the ISR.

The main idea of this work is to employ latent symmetries to construct HOTIs. Before we do so, let us discuss two important properties of latent symmetries and the ISR. Firstly, it has been recently shown that the presence of latent symmetry also implies a certain (though in general non-geometric) symmetry on the level of the original Hamiltonian [23]. Let us define the eigenvalue problem $A\mathbf{v} = \lambda\mathbf{v}$ and let $\mathcal{R}_S(A, \lambda)$ be the ISR of A. If there exist a symmetry T that becomes apparent after the ISR, that is

$$T\mathcal{R}_S(A, \lambda)T^{-1} = \mathcal{R}_S(A, \lambda), \tag{7}$$

then there also exists a symmetry on the level of A of the form $QAQ^{-1} = A$, with $Q = T \oplus \overline{Q}$, where $\overline{Q}$ is a normal matrix that acts on $\overline{S}$. Equivalently,

$$[T, \mathcal{R}_S(A, \lambda)]_- = 0 \quad \Rightarrow \quad \exists Q = T \oplus \overline{Q} : [Q, A]_- = 0, \tag{8}$$

where $[A, B]_- = AB - BA$ denotes the commutator. Two points are noteworthy here. Firstly, there is a strong connection between latent symmetries—symmetries of the isospectral reduction—and symmetries of the underlying Hamiltonian. In particular, this connection implies that one can use the tools developed for conventional symmetries also to latent ones. A good example is group theory and its connection to spectral degeneracies, which were treated in Ref. [20]. Secondly, the symmetry Q corresponding to a latent symmetry T usually has a rather complicated structure. In the latently symmetric systems presented in this work, Q is a unitary transformation, whose action is[2] not easy to interpert—as opposed to the action of a geometric symmetry, which corresponds to a permutation matrix. We shall see examples for this statement throughout the manuscript.

---

[1]For simplicity, from now on we will use $\mathfrak{h}(k)$ instead of $\mathcal{R}_S[h(k), E]$ to denote the ISR of $h(k)$. The energy dependence and reduction to S are implied.

[2]There is one exception to this statement: The isospectral reduction shown in Fig. 3(f) features a reflection symmetry about a vertical axis that goes through the upper of the three sites; the corresponding symmetry Q of the original setup [Fig. 3 (b)] is a permutation matrix.

With some additional technical preface, a reasoning similar to Eq. (8) can be applied to crystalline symmetries. Let us assume that our unit cell features a latent T symmetry (for instance, C_n) that becomes apparent after performing an ISR to the set S of its sites, i.e. $[\mathcal{R}_S(H,E), T]_- = 0$. We then build a lattice such that (i) the ISR performed on the union of sites S in all unit cells is T-symmetric, and (ii) intercell-coupling only exists between sites S. It is now easy to show the following: If we denote the reduced Bloch-Hamiltonian of the lattice by $\mathfrak{h}(k)$, we find, analogous to Ref. [10],

$$T\mathfrak{h}(\mathbf{k})T^{-1} = \mathfrak{h}(D_T\mathbf{k}), \tag{9}$$

where D_T is the representation of T on the vector space of reciprocal lattice vectors. For example, mirror symmetry ($T \equiv M$) flips spatial coordinates, such that $D_M k = -k$. The analogue of Eq. (7) is then

$$\left(T \oplus \overline{Q}\right)h(\mathbf{k})\left(T \oplus \overline{Q}\right)^{-1} = h(D_T\mathbf{k}). \tag{10}$$

To make things more specific, let us now investigate the latent SSH model introduced in Eq. (5). This model features a (1D) latent mirror symmetry: $T = M = \sigma_x$ and $D_M k = -k$. The symmetry Q of $h_{\mathrm{LSSH}}(k)$ is given by (details on the derivation of the matrix Q are given in Appendix A)

$$Q = M \oplus \overline{Q} = \begin{pmatrix} 0 & 1 & 0 & 0 \\ 1 & 0 & 0 & 0 \\ 0 & 0 & \frac{1}{\sqrt{2}} & \frac{1}{\sqrt{2}} \\ 0 & 0 & \frac{1}{\sqrt{2}} & \frac{-1}{\sqrt{2}} \end{pmatrix}. \tag{11}$$

The existence of Q is central to the analysis considered in this work. In this case, it acts as a permutation on the red sites, but as a general orthogonal transformation on the other sites. Importantly, since Q acts similarly on $h_{\mathrm{LSSH}}(k)$ as an ordinary mirror symmetry would, that is $Qh_{\mathrm{LSSH}}(k)Q^{-1} = h_{\mathrm{LSSH}}(-k)$, it poses the exact same restrictions as mirror symmetry would. For example, the Wilson loop eigenvalues ν_α of $h_{\mathrm{LSSH}}(k)$ are restricted to be 0, π or come in pairs $\{-\nu, \nu\}$. Moreover, its Zak phase φ is quantized to 0 or π. Both the Wilson loop eigenvalues and the Zak phase at different filling factors are shown in Table 1.

Table 1: Wilson loop eigenvalues ν_α and Zak phase φ for different fillings n of $h_{\mathrm{LSSH}}(k)$. For $|\nu| > 1$ the model is always trivial, while for $|\nu| < 1$ the model is topological for fillings $n = 1$ and $n = 3$.

n	$|\nu| > 1$		$|\nu| < 1$	
	ν_α	φ	ν_α	φ
1	0	0	π	π
2	$\{-\nu, \nu\}$	0	$\{-\nu, \nu\}$	0
3	$0, \{-\nu, \nu\}$	0	$\pi, \{-\nu, \nu\}$	π

Secondly, besides revealing latent symmetries, the ISR also allows for a simpler topological characterisation of Bloch Hamiltonians. More concretely, consider two Hamiltonians $h_1(\mathbf{k}, \mathbf{t} = \{t_1, t_2, \ldots, t_n\})$ and $h_2(\mathbf{k}, \mathbf{g} = \{g_1, g_2, \ldots, g_m\})$. The first one, $h_1(\mathbf{k}, \mathbf{t})$, represents a known model which exhibits a gap closing at $E = E_0$ captured through a condition on the parameters $\mathbf{t}$ that could equivalently be written as $f(\mathbf{t}) = 0$. For the SSH-model, for instance, we have $\mathbf{t} = (\nu)$ and the gap closes at $f(\nu) = 1 - |\nu| = 0$; see the example below. Let us then assume that the ISR of the second model has the same form as $h_1(\mathbf{k})$, but with energy-dependent

parameters $\{t_1(E,\mathbf{g}), t_2(E,\mathbf{g}), \ldots, t_n(E,\mathbf{g})\} \equiv \mathbf{t}(E,\mathbf{g})$, up to a constant energy-dependent shift $a(E,\mathbf{g})$,[3] i.e.,

$$\mathfrak{h}_2(\mathbf{k}) = h_1\big[\mathbf{k}, \mathbf{t}(E,\mathbf{g})\big] + a(E,\mathbf{g})\mathbb{I}. \tag{12}$$

Then, we can extract the gap closing energies, E^*, of $h_2(\mathbf{k},\mathbf{g})$ from

$$E^* - a(E^*, \mathbf{g}) = E_0. \tag{13}$$

The corresponding values of $\mathbf{g}$ can be obtained by solving $f\big[\mathbf{t}(E^*,\mathbf{g})\big] = 0$. When the ISR reduces a system to a known model, the topological characterisation of the system is reduced from calculating multiband topological invariants to solving an algebraic problem [21, 22]. As an example, consider now the latent SSH model described by Eq. (5). The 'ordinary' SSH model has a gap closing at $E_0 = 0$ for $f(v) = 1 - |v| = 0$. The gap closing energies E^* for the latent model are thus determined through

$$E^* - a(E^*, w) = E^* - \frac{2w^2}{E^*} = 0. \tag{14}$$

Equation 14 has two solutions $E^* = \pm\sqrt{2}w$, which is corroborated by Fig. 1(d) showing two sets of in-gap modes in red. The energies E^* predict the topological phase transition through $f[s(E^*,w)] = 1 - |s(E^*,w)| = 0$, which in this case reduces to $|w| = 1$, akin to the SSH model. One can also conclude that in order to respect the symmetries of the system at bulk insulating filling, the system with OBC must feature a filling-anomaly.

2.2 Further perspectives on latent symmetries

Classifying symmetries in physics often involves a nuanced and somewhat arbitrary distinction. Typically, "obvious" symmetries are those identifiable by an experienced physicist through a detailed examination of the system. These include geometric operations like reflection, rotation, inversion, and their combinations. However, while predominantly encompassing geometric symmetries, this category does not cover all potential symmetries of a given Hamiltonian h.

A perfect example of the prevalence of such an (arbitrary) classification into obvious and non-obvious (often called "hidden") symmetries are spectral degeneracies: In group theory, one can make a strong link between the spectral degeneracies of h and the group that is formed by its symmetries. In particular, through Schur's lemma, the number and dimension of the so-called irreducible representations of the group are directly linked to the degeneracies of the Hamiltonian. Importantly, it might be that not all (or even none) of the degeneracies of the Hamiltonian can be explained from the group-theoretical analysis of its obvious symmetries. In this case, the degeneracies are colloquially said to be "accidental", though they can be easily explained by considering the non-obvious (hidden) symmetries as well. A pedagogical discussion of how "accidental" double degeneracies can easily be explained has been done in Ref. [24]. For a deeper discussion, including a list of physical setups featuring accidental degeneracies, see, for instance, Ref. [25].

There are, nevertheless, good reasons behind the (arbitrary) division into obvious and non-obvious (or hidden) symmetries. Perhaps the most important reason is the following. Usually, the symmetries of a Hamiltonian are used to simplify the eigenvalue problem $h\psi = E\psi$. For instance, if h is reflection-symmetric, one can deduce that its eigenvectors have definite parity. This knowledge can then be used to split the original eigenvalue problem into two smaller, easier-to-solve problems. Overall, any obvious symmetry of h is of high value in solving eigenvalue problems. On the other hand, symmetries that are difficult to find—for instance, by first diagonalizing h, that is, performing the expensive task that one wanted to simplify in the first place—are usually not helpful in simplifying eigenvalue problems.

---

[3]Recall that through the ISR, the reduced parameters depend on both energy E and the original system parameters $\mathbf{g}$.
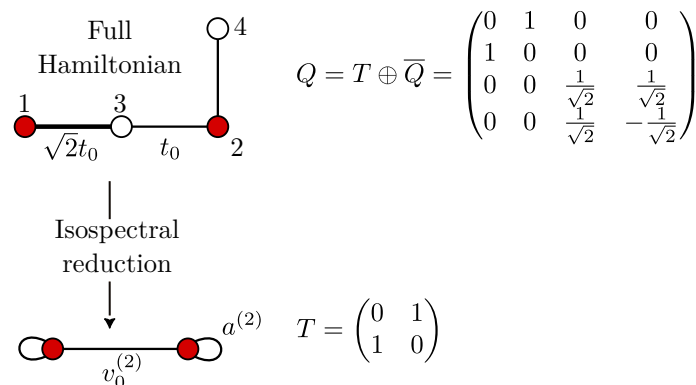
Figure 2: A latently C_2-symmetric setup, along with the relevant matrices Q and T (see text for details). The four sites of the original Hamiltonian are labeled 1 to 4.

Let us finally discuss the role of latent symmetries. As we have seen already in Eq. (7), if a Hamiltonian h has a latent symmetry T on a set of sites S, that is, $[\mathcal{R}_S(h), T] = 0$, then the full Hamiltonian h possesses a symmetry $Q = T \oplus \overline{Q}$. This means that any latent symmetry corresponds to a full symmetry, as was already implied in Eq. (8). On the one hand, this is beneficial since it allows one to use all of the machinery developed for normal symmetries to latent ones. On the other hand, one might be tempted to say that they are not new at all. To judge their relevance and novelty better, let us go back to the example discussed above, that is, the system depicted in Fig. 1 (c). The Hamiltonian of the unit cell of this lattice is depicted again in Fig. 2. Just as the Bloch-Hamiltonian of the full lattice, Eq. (5), the unit cell Hamiltonian clearly has no geometric symmetry, while its isospectral reduction, depicted below the original setup, is reflection-symmetric. According to the above discussion, the original setup would most likely be considered "asymmetric". We emphasize that the symmetry Q, which corresponds to the latent reflection symmetry and is the same as in Eq. (11), corroborates this perceived asymmetry. Indeed, Q—which we also show in Fig. 2—is difficult to interpret; it looks like a rather generic orthogonal transformation. At this point, let us emphasize that—in the context of a conventional tight-binding system—a "conventional" (spatial) symmetry usually can be mapped to a permutation matrix. The matrix Q, however, is clearly not of this type. We note that the above discussion can be done in a similar manner for all the latently symmetric unit cells we present in the subsequent sections. Moreover, this discussion can be repeated (though in a more complicated manner, but with the same outcome) when embedding those unit cells into a lattice.

Latent symmetries lie somewhat between fully obvious symmetries (like the geometric ones) and highly non-obvious symmetries, which are both difficult to find and interpret. Indeed, in the above example, Q is a rather abstract orthogonal operation, while T is a permutation matrix that can be directly related to a reflection. The translation between these two worlds—the abstract, and the concrete—is done by means of the isospectral reduction, which serves as a powerful tool to eliminate the complexity. These two new tools, the isospectral reduction and latent symmetries, further weaken the artificial divide between obvious and non-obvious symmetries.

3 Topological indices from (latent) rotational symmetry

In the above, we have discussed a simple latent SSH model, which has been previously investigated both in its Hermitian [21] and its non-Hermitian [22] version. In the remainder of

this work, we apply a similar reasoning to develop the concept of *latent HOTIs*. To this end, we start by reviewing the existing methods for the classification of usual HOTIs. We focus on two-dimensional insulators that preserve time-reversal symmetry (class AI in the Altland-Zirnbauer classification [1,2]). The introduction of crystalline symmetries allows for a further classification of these materials [6,26]. Here, we will follow Ref. [14].

3.1 Recap: Topological indices through conventional geometric rotation symmetries

The presence of a rotation symmetry $\hat{C}_n$, which rotates sites in a lattice by $2\pi/n$ rad around some point, is represented on the level of the Bloch Hamiltonian by

$$\hat{C}_n h(\mathbf{k}) \hat{C}_n^{-1} = h(D_{C_n} \mathbf{k}), \tag{15}$$

where, similar to Eq. (9), D_{C_n} is a linear transformation on $\mathbf{k}$ that depends on C_n. At high symmetry points (HSPs) in the Brillouin zone, i.e. points that are mapped to themselves (modulo a reciprocal lattice vector), $D_{C_n} \mathbf{\Pi}^{(n)} = \mathbf{\Pi}^{(n)}$, we have

$$\left[\hat{C}_n, h\left(\mathbf{\Pi}^{(n)} \right) \right]_- = 0. \tag{16}$$

Because $\hat{C}_n$ and $h(k)$ commute at a HSP $\mathbf{\Pi}^{(n)}$, they share an eigenbasis. Thus, the Bloch states $\left| u(\mathbf{k} = \mathbf{\Pi}^{(n)}) \right\rangle$ can be chosen as eigenstates of $\hat{C}_n$, such that

$$\hat{C}_n \left| u\left(\mathbf{\Pi}^{(n)} \right) \right\rangle = \Pi_p^{(n)} \left| u\left(\mathbf{\Pi}^{(n)} \right) \right\rangle. \tag{17}$$

Since $\left(\hat{C}_n \right)^n = \mathbb{I}$, its eigenvalues are the n-th roots of unity:

$$\Pi_p^{(n)} = e^{\frac{2\pi i}{n}(p-1)}, \quad \text{with} \quad p \in \{1, 2, \dots n\}. \tag{18}$$

From these eigenvalues, we can construct rotation topological invariants of the form

$$\left[\Pi_p^{(n)} \right] \equiv \#\Pi_p^{(n)} - \#\Gamma_p^{(n)}, \tag{19}$$

where $\#\Pi_p^{(n)}$ denotes the number of bands below the energy gap with eigenvalue $\Pi_p^{(n)}$ and $\mathbf{\Gamma} = \mathbf{0}$ is the gamma point in the Brillouin zone, which is a natural reference point to calculate the rotational invariants.[4] $[\Pi_p^{(n)}]$ characterises the topology of C_n-symmetric insulators in a similar way to inversion eigenvalues: A difference of inversion eigenvalues between two HSPs indicates band inversion, i.e. non-trivial topology. In a similar manner, the difference of rotation eigenvalues between HSPs, captured by $[\Pi_p^{(n)}]$, allows for a comparison of the representations of rotation symmetry. If different representations exist, the energy bands exhibit non-trivial topology. As a consequence of TRS and the fact that the number of bands is constant through the Brillouin zone, one obtains a set of independent topological indices $\chi^{(n)}$ for C_n-symmetric materials [14],

$$\begin{aligned}
\chi^{(2)} &= \left(\left[X_1^{(2)} \right], \left[Y_1^{(2)} \right], \left[M_1^{(2)} \right] \right), \\
\chi^{(4)} &= \left(\left[X_1^{(2)} \right], \left[M_1^{(4)} \right], \left[M_2^{(4)} \right] \right), \\
\chi^{(3)} &= \left(\left[K_1^{(3)} \right], \left[K_2^{(3)} \right] \right), \\
\chi^{(6)} &= \left(\left[M_1^{(2)} \right], \left[K_1^{(3)} \right] \right).
\end{aligned} \tag{20}$$

---

[4]$\mathbf{\Pi}$ (Π) should be viewed as a 'placeholder'. It will take the values $\mathbf{X}, \mathbf{Y}, \mathbf{M}, \mathbf{K}$ and $\mathbf{K}'$ (X, Y, M, K and K'). For example, $[K_2^{(3)}]$ represents the number of eigenvalues of $\hat{C}_3 |u(\mathbf{K})\rangle$ that are equal to $\exp\{2\pi i/3\}$, minus the number of eigenvalues evaluated at the $\mathbf{\Gamma}$ point.

3.2 Topological indices through latent rotation symmetries

Having reviewed the theory regarding geometric symmetries, let us now discuss how latent symmetries fit into the scheme. Rather surprisingly, it can be shown that the invariants $\chi^{(n)}$ are still applicable. The key for this insight is Eq. (8). Equipped with this equation, one only needs to replace the symmetry operator $\hat{C}_n$ in Eq. (17) by $\hat{C}_n \oplus \overline{Q}$, as defined in Eq. (10). Upon doing so, the rotation invariants of latent symmetric models can be evaluated to characterize the topology of the system. This leads to the definition of latent rotation symmetric HOTIs through

$$\left[\hat{C}_n \oplus \overline{Q}, h\left(\mathbf{\Pi}^{(n)}\right)\right]_- = 0, \tag{21}$$

where the total symmetry $\hat{C}_n \oplus \overline{Q}$ is not necessarily geometric. Equivalently, we have

$$\left[\hat{C}_n, \mathfrak{h}\left(\mathbf{\Pi}^{(n)}\right)\right]_- = 0. \tag{22}$$

3.3 Classification of HOTIs: Dipole moment and corner charges

The rotation invariants $\chi^{(n)}$ can be related to physical properties of the systems, such as the dipole moment $\mathbf{P}^{(n)}$ and corner charge $Q^{(n)}$. These quantities are derived in Ref. [14] for geometric symmetries and can be easily shown to hold also for latent symmetries.

Below, we will directly state the results for the dipole moment,

$$\mathbf{P}^{(2)} = \frac{e}{2}\left(\left[Y_1^{(2)}\right] + \left[M_1^{(2)}\right]\right)\mathbf{a_1} + \frac{e}{2}\left(\left[X_1^{(2)}\right] + \left[M_1^{(2)}\right]\right)\mathbf{a_2},$$

$$\mathbf{P}^{(4)} = \frac{e}{2}\left[X_1^{(2)}\right](\mathbf{a_1} + \mathbf{a_2}),$$

$$\mathbf{P}^{(3)} = \frac{2e}{3}\left(\left[K_1^{(3)}\right] + 2\left[K_2^{(3)}\right]\right)(\mathbf{a_1} + \mathbf{a_2}),$$

$$\mathbf{P}^{(6)} = \mathbf{0}, \tag{23}$$

and for the corner charge,

$$Q^{(2)} = \frac{e}{4}\left(-\left[X_1^{(2)}\right] - \left[Y_1^{(2)}\right] + \left[M_1^{(2)}\right]\right),$$

$$Q^{(4)} = \frac{e}{4}\left(\left[X_1^{(2)}\right] + 2\left[M_1^{(4)}\right] + 3\left[M_2^{(4)}\right]\right),$$

$$Q^{(3)} = \frac{e}{3}\left[K_2^{(3)}\right],$$

$$Q^{(6)} = \frac{e}{4}\left[M_1^{(2)}\right] + \frac{e}{6}\left[K_1^{(3)}\right]. \tag{24}$$

The dipole moments are defined modulo e/A_{cell} times a lattice vector and the corner charges are defined modulo e. Here A_{cell} denotes the area of the unit cell. Notice also that we group the dipole moments $\mathbf{P}^{(2)}$ and $\mathbf{P}^{(4)}$ ($\mathbf{P}^{(3)}$ and $\mathbf{P}^{(6)}$) because they share at least one common topological index (the same is done for the corner charges as well).

Before we continue, let us briefly remind the reader about the connection between these two quantities and HOTIs. To this end, we consider a system under OBC, terminated respecting its (latent or geometric) C_n symmetry. The system is a HOTI if it is (higher order) topological and insulating. The former requirement translates in a nonzero corner charge. If the dipole moment $\mathbf{P}^{(n)}$ does not vanish, there will be in-gap states when OBC are imposed. This poses two constraints on a HOTI, be it conventional or latent:

- The corner charge $Q^{(n)}$, as given by Eq. (24), is nonzero.

- The dipole moment $\mathbf{P}^{(n)}$, as given by Eq. (23), vanishes.

In the remainder of this manuscript, we will show how one can construct a latent HOTI, that is, a latently C_n-symmetric system fulfilling these two criteria.
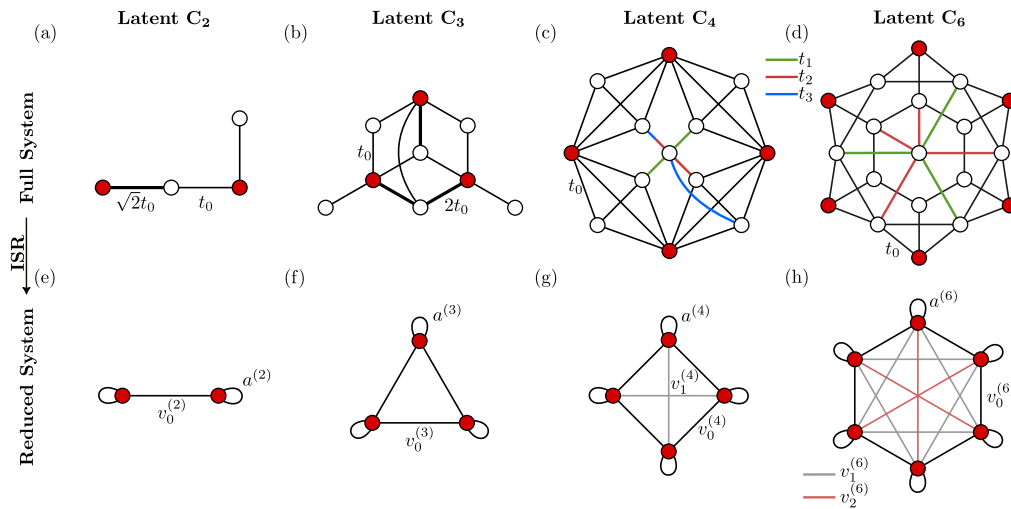
Figure 3: Latently C_n symmetric unit cells. (a-d) Minimal examples of unit cells that show a latent C_2, C_3, C_4, and C_6 symmetry without a direct geometric symmetry. Relevant hopping parameters are indicated. (e-h) Cells obtained upon performing an ISR to the red sites of the unit cells in (a-d), the reduced systems show geometric C_n symmetries, revealing the latent symmetries in (a-d). Relevant (energy-dependent) parameters are indicated.

4 Building blocks for latent HOTIs

A necessary first step to construct a latent HOTI is a sufficiently large set of latently C_n symmetric lattices. In this section, we start by showing how they can be built in subsection 4.1.

Afterwards, we introduce specific examples of unit cells that feature a latent C_2-, C_3-, C_4-, and C_6-symmetry, as depicted in Fig. 3. Then, in subsection 4.2 we shall use these unit cells to construct lattices such that the total system retains the latent C_n rotation symmetry. Finally, in subsection 4.3, we present a systematic way of constructing latently C_n-symmetric setups with a pre-defined topological index. Equipped with all these tools, we will then finally construct latent HOTIs in Section 5.

4.1 Latently symmetric unit cells

In the following, we will present unit cells featuring a latent C_2, C_3, C_4, or C_6 symmetry. We emphasize that each of them is just a specific example of a large class of unit cells featuring these latent symmetries. Before we continue, let us explain how these families of latently C_n symmetric unit cells can be designed.

For the design of latently C_2-symmetric unit cells, there are different techniques that range from exhaustive search [27] to more sophisticated graph-theoretical results [28]. The interested reader is referred to the literature on graphs[5] with cospectral vertices [28, 29]; every graph with this property has recently been shown to have a latent C_2-symmetry [18]. The four-site latently C_2-symmetric cell that we depict in Fig. 3(a) was found analytically by starting with a four-site long chain with couplings a, b, c and all on-site energies equal to zero. Then, demanding that two sites u, v in this chain are latently symmetric, analytical expressions for the three couplings were found.

---

[5]We note that there is a one-to-one mapping between a graph and its adjacency matrix H, which for many graphs is Hermitian and could thus be interpreted as a Hamiltonian.

The construction of unit cells with a latent C_3, C_4, and C_6-symmetry is more demanding, but can be done using the complement multiplet technique explained in the Supplemental Material of Ref. [20]. This technique starts with a Hamiltonian that features a geometric C_n symmetry. As can be easily shown, such a Hamiltonian likewise features a latent C_n symmetry.[6] By carefully analyzing its matrix powers, sets of changes to the Hamiltonian can be identified that keep the latent C_n symmetry. In many cases, however, these changes break the initial geometric C_n symmetry, thus resulting in a purely latently C_n symmetric Hamiltonian. In this manner, the setups depicted in Fig. 3(b), (c), and (d) have been found.

Having discussed how latently C_n-symmetric unit cells can be designed, let us now investigate specific examples of these.

4.1.1 Latent C_2 symmetry

In Sec. 2, the notion of a latently mirror symmetric system was introduced in the context of the latent SSH model. In 1D, C_2 and mirror symmetry are the same, hence we take the latent SSH unit cell as a building block for latent C_2-symmetric HOTIs. The unit cell of the latent SSH model, and its ISR to the red sites, are once more displayed in Figs. 3(a) and 3(e), respectively. The Hamiltonian for the single cell in Fig. 3(a) is given by

$$H_L^{(2)} = t_0 \begin{pmatrix} 0 & 0 & \sqrt{2} & 0 \\ 0 & 0 & 1 & 1 \\ \sqrt{2} & 1 & 0 & 0 \\ 0 & 1 & 0 & 0 \end{pmatrix}. \tag{25}$$

The parameters in the isospectrally reduced model in Fig. 3(e) are given by $a^{(2)} = 2t_0^2/E$ and $v_0^{(2)} = \sqrt{2}t_0^2/E$. The reduced model obeys a C_2-symmetry,

$$\hat{C}_2 = \begin{pmatrix} 0 & 1 \\ 1 & 0 \end{pmatrix}, \tag{26}$$

which corresponds to the symmetry,

$$Q^{(2)} \equiv \hat{C}_2 \oplus \overline{Q}^{(2)} = \begin{pmatrix} 0 & 1 \\ 1 & 0 \end{pmatrix} \oplus \begin{pmatrix} \frac{1}{\sqrt{2}} & \frac{1}{\sqrt{2}} \\ \frac{1}{\sqrt{2}} & -\frac{1}{\sqrt{2}} \end{pmatrix}, \tag{27}$$

of the full Hamiltonian.

4.1.2 Latent C_3 symmetry

An example of a unit cell exhibiting latent C_3 symmetry is depicted in Fig. 3(b). It has 9 sites, with hopping given by t_0 (thin black lines) and $2t_0$ (thick black lines). Its Hamiltonian is given by

$$H_L^{(3)} = t_0 \begin{pmatrix} 0 & 0 & 0 & 1 & 1 & 1 & 2 & 0 & 0 \\ 0 & 0 & 0 & 0 & 1 & 2 & 1 & 1 & 0 \\ 0 & 0 & 0 & 1 & 0 & 2 & 1 & 0 & 1 \\ 1 & 0 & 1 & 0 & 0 & 0 & 0 & 0 & 0 \\ 1 & 1 & 0 & 0 & 0 & 0 & 0 & 0 & 0 \\ 1 & 2 & 2 & 0 & 0 & 0 & 0 & 0 & 0 \\ 2 & 1 & 1 & 0 & 0 & 0 & 0 & 0 & 0 \\ 0 & 1 & 0 & 0 & 0 & 0 & 0 & 0 & 0 \\ 0 & 0 & 1 & 0 & 0 & 0 & 0 & 0 & 0 \end{pmatrix}. \tag{28}$$

---

[6]This can be shown by performing the isospectral reduction on any n sites that are mapped onto each other by the corresponding symmetry operator C_n commuting with the underlying Hamiltonian.

Upon performing an ISR to the red sites, the cell shown in Fig. 3(f) is obtained, displaying a C_3-symmetry. The reduced model has a single energy-dependent hopping parameter $v_0^{(3)} = 5t_0^2/E$ and onsite potential $a^{(3)} = 7t_0^2/E$.[7] The corresponding symmetry matrix of the full Hamiltonian $Q^{(3)}$ [cf. Eq. (8)] of the full system depicted in Fig. 3(b) is given by

$$Q^{(3)} \equiv \hat{C}_3 \oplus \overline{Q}^{(3)} = \begin{pmatrix} 0 & 0 & 1 \\ 1 & 0 & 0 \\ 0 & 1 & 0 \end{pmatrix} \oplus \begin{pmatrix} \frac{1}{2} & 0 & \frac{1}{2} & -\frac{1}{2} & \frac{1}{2} & 0 \\ \frac{1}{2} & \frac{1}{2} & 0 & 0 & -\frac{1}{2} & \frac{1}{2} \\ 0 & \frac{1}{2} & \frac{1}{2} & \frac{1}{2} & 0 & -\frac{1}{2} \\ 0 & -\frac{1}{2} & \frac{1}{2} & \frac{1}{2} & 0 & \frac{1}{2} \\ \frac{1}{2} & 0 & -\frac{1}{2} & \frac{1}{2} & \frac{1}{2} & 0 \\ -\frac{1}{2} & \frac{1}{2} & 0 & 0 & \frac{1}{2} & \frac{1}{2} \end{pmatrix}. \tag{29}$$

4.1.3 Latent C_4 symmetry

Next, let us investigate the setup shown in Fig. 3(c), which has 13-sites and features four different hopping parameters: t_0 (black), t_1 (green), t_2 (red), and t_3 (blue). A double-coloured line implies a sum of the two hopping strengths, i.e. the blue-and-red line has hopping parameter $t_2 + t_3$. The matrix form, $H_L^{(4)}$, of Fig. 3(c) is given in Appendix B.1 by Eq. (B.1). Depending on the choice of couplings, this unit cell has different geometric symmetries. Firstly, if $t_1 = t_2$ and $t_3 = 0$, it enjoys a C_4-symmetry. Keeping $t_3 = 0$ but breaking the equality of the first two couplings such that $t_1 \neq t_2$, this symmetry is partly broken and only a geometric C_2 symmetry is left. The situation becomes much easier, though, when performing an ISR on the red sites. The resulting reduced model is depicted in Fig. 3(g); it has an energy-dependent on-site potential $a^{(4)}$ and hopping parameters $v_0^{(4)}$ (black) and $v_1^{(4)}$ (grey). As can be easily checked, it has a C_4 symmetry given by

$$\hat{C}_4 = \begin{pmatrix} 0 & 0 & 0 & 1 \\ 1 & 0 & 0 & 0 \\ 0 & 1 & 0 & 0 \\ 0 & 0 & 1 & 0 \end{pmatrix}. \tag{30}$$

Thus, regardless of the choice of couplings t_i, the unit cell is latently C_4-symmetric. Once again, this demonstrates that the ISR gives a wider, more comprehensive viewpoint on a system than merely checking its geometric symmetries. Before continuing, we remark that—again, by Eq. (8)—this latent C_4 symmetry corresponds to a non-geometric symmetry $Q^{(4)} \equiv \hat{C}_4 \oplus \overline{Q}^{(4)}$ of the full unit cell.

Expressions for $\overline{Q}^{(4)}$ and the parameters in Fig. 3(g) are given in Appendix B.1.

4.1.4 Latent C_6 symmetry

Finally, we come to the unit cell depicted in Fig. 3(d). It has 19 sites and features three different hopping parameters t_0 (black), t_1 (green), t_2 (red). A more complex latent C_6-symmetric unit cell is given in Appendix B.2. This model is C_6-symmetric only when $t_1 = t_2 = 0$. Furthermore, it is C_3 symmetric if only $t_2 = 0$. Once again, the picture becomes clearer when performing an ISR to the red sites. The resulting reduced model is depicted in Fig. 3(h); it is described in terms of the on-site potential $a^{(6)}$ and hopping parameters $v_0^{(6)}$ (black), $v_1^{(6)}$ (grey), and $v_2^{(6)}$ (red). It can be promptly seen that the reduced model is C_6-symmetric. Thus, irrespective of the choice of coupling parameters t_i, the full unit cell is latently C_6-symmetric. This latent symmetry

---

[7]For brevity, we have dropped the energy dependence in the notation of the reduced hopping parameter and onsite potential: $v_i^{(n)} = v_i^{(n)}(E)$ and $a^{(n)} = a^{(n)}(E)$.

corresponds to a non-geometric symmetry of the full unit cell, given by $Q^{(6)} \equiv \hat{C}_6 \oplus \overline{Q}^{(6)}$, with full expressions for $\overline{Q}^{(6)}$ and the parameters in Fig. 3(h) given in Appendix B.2.

4.2 Lattice structures preserving latent C_n-symmetries

Equipped with a set of latently C_n-symmetric unit cells, the next step is to embed these into lattices, such that the total setup keeps this symmetry. As we now show, this task is rather simple. Let us assume that a given lattice structure is composed of a unit cell with a geometric C_n-symmetry, such that the lattice as a whole keeps the symmetry. Next, let us replace the geometrically C_n-symmetric unit cell by one whose ISR on a set S of sites has the same symmetry, i.e. a latently C_n-symmetric unit cell. It is then a trivial task to show that the lattice's ISR—for clarity, we mean the simultaneous reduction on the union of sites S in each unit cell—is C_n-symmetric. In other words, the lattice is latently C_n-symmetric.

Examples of systems with these features are discussed in more detail in the following section.

4.3 Primitive generators and their topological classification

With the material presented so far, one could easily construct a large number of latently C_n-symmetric lattices. However, to be HOTIs, they need a vanishing dipole moment and a non-vanishing corner charge. Via Eqs. (23) and (24), both quantities are connected to the topological indices in Eq. (20). In principle, one could then find latent HOTIs by a brute-force search, that is, by computing these quantities for a large number of latently C_n-symmetric setups and filtering out the ones that are HOTIs. However, there is a more elegant and systematic way that is based on the concept of *primitive generators* [14]. Essentially, these are building blocks with certain properties, which can be connected to each other in a specific manner, such that the resulting setup features a well-defined topological index.

To introduce these generators, let us start with an interesting fact on topological indices. As pointed out in Ref. [14], two models with the same C_n-symmetry, described by Bloch Hamiltonians h_1 and h_2, characterized by $\chi_1^{(n)}$ and $\chi_2^{(n)}$, respectively, may be combined to form a third model

$$h_3 = \begin{pmatrix} h_1 & \gamma \\ \gamma^\dagger & h_2 \end{pmatrix}. \tag{31}$$

Here, γ connects the two different Hamiltonians in a way that does not close any gaps and that preserves C_n-symmetry. The rotation invariant of the new model is then given by $\chi_3^{(n)} = \chi_1^{(n)} + \chi_2^{(n)}$. Consequently, if for a given symmetry $\chi^{(n)}$ has N components, it is sufficient to have N models with linearly independent $\chi^{(n)}$ to span the whole topological phase space. This sets the basis to the notion of *primitive generators*. The primitive generators form a minimal set from which a setup with an arbitrary topological index can be constructed. From there, the construction of an actual (latent) HOTI is only a minor step.

In the following, we will discuss and classify (latent) primitive generators for every one of the four classes C_2, C_3, C_4, and C_6 that are compatible with translational invariance of a crystal. The key results are graphically depicted in Figs. 4 to 7 and are discussed in more detail in the text. For each of the four classes, we first treat the conventional case of geometric symmetry, and then treat the new case of latent symmetry. This dual treatment might seem redundant, but it serves two purposes. Firstly, the characteristics (for instance, the band structure) of the geometric and latent setups have some striking similarity that would otherwise be unnoticed. Secondly, our treatment of the geometrically symmetric primitive generators represents minor generalisations of the primitive generators introduced in Ref. [14].

In each of the following examples, the primitive generators are the Bloch-Hamiltonians of a crystal obtained by inserting a specific unit cell (with either a geometric or latent C_n symmetry) into a specific lattice structure. We remark that a given C_n might support different lattice structures.

4.3.1 C_2-symmetry

For a C_2 symmetry, we investigate only one lattice structure, which we call the "stacked SSH model".

Geometric stacked SSH. We consider the primitive generator given by the Hamiltonian

$$h_1^{(2)}(\mathbf{k}) = \begin{pmatrix} 2w\cos k_y & t + e^{ik_x} \\ t + e^{-ik_x} & 2w\cos k_y \end{pmatrix}. \tag{32}$$

It is the Bloch-Hamiltonian of a system obtained by inserting the unit cell depicted in Fig. 4(a) into the stacked SSH lattice structure of Fig. 4(d). The system corresponds to multiple SSH chains stacked in the y-direction. Hopping within a chain occurs with an intracell hopping given by t (solid black line) and a horizontal intercell hopping of 1 (dashed black line). The chains are connected with a vertical intercell hopping of w (dot-dashed black line). The lattice vectors are given by $\mathbf{a_1} = (1,0)$ and $\mathbf{a_2} = (0,1)$. Eq. (32) admits a C_2-symmetry given by

$$\hat{C}_2 h_1^{(2)}(k_x, k_y)\hat{C}_2^{-1} = h_1^{(2)}(-k_x, -k_y), \tag{33}$$

where $\hat{C}_2$ is given by Eq. (26). Consequently, the topology of the system may be characterized using $\chi^{(2)}$. Since the value of w does not affect the gap structure, we set $w = 0$. For general values of t, the spectrum is gapped at half filling, as shown in Fig. 4(b), giving rise to two distinct phases. These phases are separated by a gap closing at $t = +1$ (-1), taking place along the **XM** (**YΓ**) path in the Brillouin zone. For $|t| < 1$, the system is in its topological phase, corresponding to $\chi^{(2)} = (1,0,1)$ and $\mathbf{P}^{(2)} = (e/2)\mathbf{a_1}$. For $|t| > 1$, the system is trivial with $\chi^{(2)} = (0,0,0)$ and $\mathbf{P}^{(2)} = \mathbf{0}$. The different topological phases are depicted in Fig. 4(c). We note that a second, independent, generator for C_2 can be obtained by rotating Fig. 4(d) by 90 degrees. This would correspond by letting $k_x \to k_y$ and $k_y \to -k_x$ in Eq. (32). As a result, the topological phase would now have $\chi^{(2)} = (0,1,1)$ and $\mathbf{P}^{(2)} = (e/2)\mathbf{a_2}$. This would yield 2 generators for C_2-symmetric systems. A third generator can be obtained by taking one of the C_4 generators in the next section and making the hopping in the $x-$ and $y-$direction different.

Latent stacked SSH. If we insert the unit cell depicted in Fig. 4(e) into the lattice structure of Fig. 4(d), we obtain a system with a Bloch-Hamiltonian given by

$$h_{L,1}^{(2)}(\mathbf{k}) = H_L^{(2)} + \begin{pmatrix} 2w\cos k_y & e^{ik_x} & 0 & 0 \\ e^{-ik_x} & 2w\cos k_y & 0 & 0 \\ 0 & 0 & 0 & 0 \\ 0 & 0 & 0 & 0 \end{pmatrix}. \tag{34}$$

In Fig. 4(e), the horizontal intercell hopping (dashed black line) is fixed to 1 and the vertical intercell hopping (dot-dashed black line) is given by w. Figure 4(f) depicts the spectrum of Eq. (34) for $t_0 = 1/2$ and $w = 0$. Notice that the spectrum resembles two copies of the one in Fig. 4(b). Since this primitive generator represents stacked (latent) SSH chains, its phase diagram is the same as that of the SSH chain. At the end of Sec. 2, we showed that for this specific latent SSH model, phase transitions occur at $|t| = 1$, just like for the SSH model (again,

the value of w does not affect the gap structure). Following this reasoning, $h_{L,1}^{(2)}(\mathbf{k})$ has a gap closing at $|t_0| = 1$, separating the trivial phase $\chi^{(2)} = (0,0,0)$ ($|t_0| > 1$) from the topological phase $\chi^{(2)} = (1,0,1)$ ($|t_0| < 1$), as shown in the phase diagram in Fig. 4(g).

4.3.2 C_4-symmetry

For a C_4-symmetry, we consider three lattice structures: a "2D SSH", a "breathing square-octagon", and a "stacked breathing square-octagon".
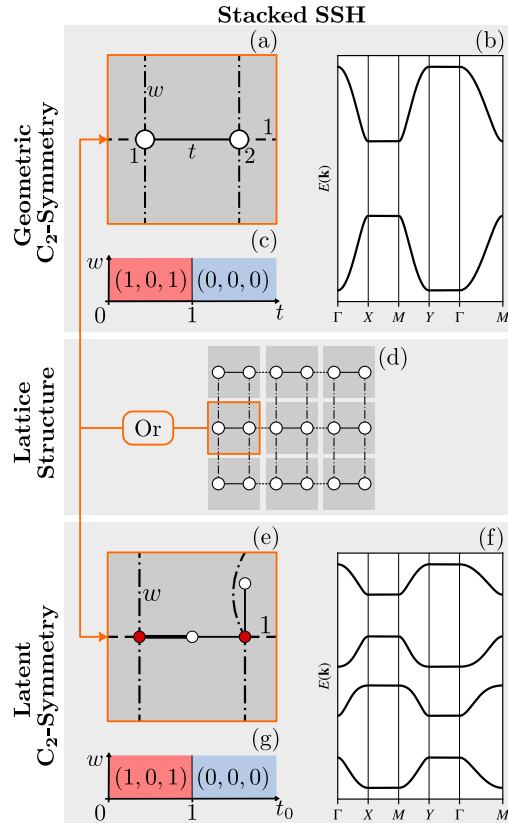

Figure 4: (a) Unit cell of the geometric C_2-symmetric primitive generator $h_1^{(2)}(\mathbf{k})$, with intracell hopping t. Horizontal intercell hopping is indicated by dashed lines and is fixed to 1; vertical intercell hopping is represented by a dot-dashed line and is given by w. (b) Energy spectrum of $h_1^{(2)}(\mathbf{k})$ for $t = 1/2$ and $w = 0$. (c) Phase diagram, in which the rotation invariants $\chi^{(2)}$ are shown for gapped phases. (d) Lattice structure of the C_2-symmetric primitive generators. The lattice represents stacked 1D SSH chains. (e) Unit cell of the Latent C_2-symmetric primitive generator $h_{L,1}^{(2)}(\mathbf{k})$. Values of the hopping parameters are indicated in Fig. 3(a) and horizontal intercell hoppings (dashed lines) are fixed to 1 while vertical intercell hopping (dot-dashed lines) are given by w. (f) Spectrum of $h_{L,1}^{(2)}(\mathbf{k})$ for $t_0 = 1/2$ and $w = 0$. (g) Phase diagram at one filled band. Rotation invariants $\chi^{(2)}$ are displayed for gapped phases.
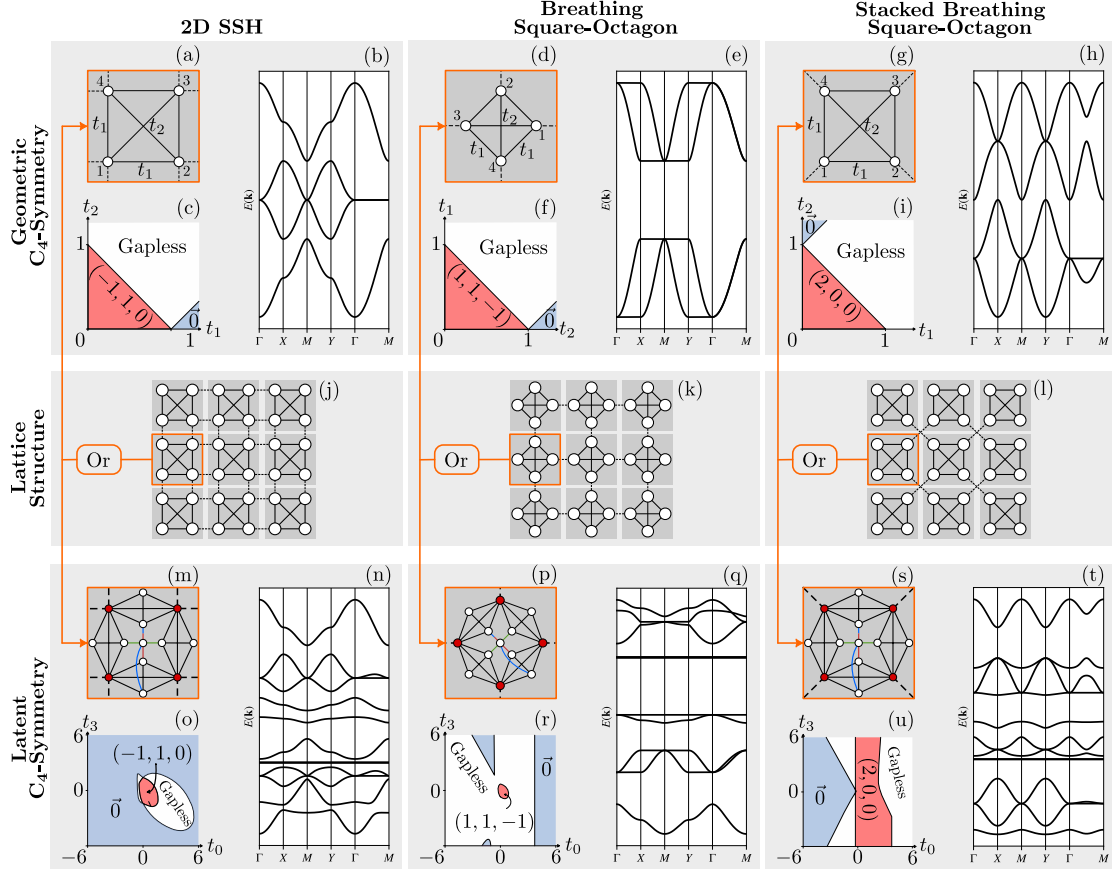
Figure 5: (a,d,g) Unit cells of the geometric C_4-symmetric primitive generators $h_1^{(4)}(\mathbf{k})$, $h_2^{(4)}(\mathbf{k})$, and $h_3^{(4)}(\mathbf{k})$, respectively. The nearest-neighbour hoppings are represented by t_1; the next-nearest-neighbour hoppings are represented by t_2; the intercell hoppings are indicated by dashed lines and are fixed to be equal to 1. (b,e,h) Energy spectra of $h_1^{(4)}(\mathbf{k})$ at $t_1 = 1/2$ and $t_2 = 0$, $h_2^{(4)}(\mathbf{k})$ at $t_1 = 1/2$ and $t_2 = 0$, and $h_3^{(4)}(\mathbf{k})$ at $t_1 = 0$ and $t_2 = 1/2$. (c,f,i) Phase diagrams of the geometric primitive generators. For gapped phases, the rotation invariants $\chi^{(4)}$ are shown. (j,k,l) Lattice structures of the C_4-symmetric primitive generators. The lattices represent a 2D SSH, a breathing square-octagon, and a stacked breathing square octagon lattice, respectively. (m,p,s) Unit cells of the latent C_4-symmetric primitive generators $h_{L,1}^{(4)}(\mathbf{k})$, $h_{L,2}^{(4)}(\mathbf{k})$, and $h_{L,3}^{(4)}(\mathbf{k})$, respectively. Values of the hopping parameters are indicated in Fig. 3(c) and intercell hoppings (dashed lines) are fixed to 1. (n,q,t) Energy spectra of $h_{L,1}^{(4)}(\mathbf{k})$ for $t_0 = t_1 = t_2 = 1$, $t_3 = 1/2$, $h_{L,2}^{(4)}(\mathbf{k})$ for $t_0 = t_1 = t_2 = 1/2$, $t_3 = 1$, and $h_{L,3}^{(4)}(\mathbf{k})$ for $t_0 = t_1 = t_2 = -1$, $t_3 = 0$. (o,r,u) Phase diagrams of $h_{L,1}^{(4)}(\mathbf{k})$ at 1 filled band, $h_{L,2}^{(4)}(\mathbf{k})$ at 2 filled bands, and $h_{L,3}^{(4)}(\mathbf{k})$ at 3 filled bands, as a function of t_0 and t_3, $t_1 = t_2 = t_0$. Rotation invariants $\chi^{(4)}$ are shown for gapped phases.

Geometric 2D SSH. Inserting the unit cell of Fig. 5(a) into a lattice structure, we obtain Fig. 5(j), which corresponds to a system described by the Bloch-Hamiltonian

$$h_1^{(4)}(\mathbf{k}) = \begin{pmatrix} 0 & t_1 + e^{ik_x} & t_2 & t_1 + e^{ik_y} \\ t_1 + e^{-ik_x} & 0 & t_1 + e^{ik_y} & t_2 \\ t_2 & t_1 + e^{-ik_y} & 0 & t_1 + e^{-ik_x} \\ t_1 + e^{-ik_y} & t_2 & t_1 + e^{ik_x} & 0 \end{pmatrix}. \tag{35}$$

The system has 4 sites per unit cell, as depicted in Fig. 5(a), and is also known as the 2D SSH model [30–32]. The sites are connected with hopping parameters t_1 and t_2 for nearest-neighbour and next-nearest-neighbour hopping, respectively. The intercell hopping (dashed lines) is fixed to unity. The lattice vectors are given by $\mathbf{a_1} = (1,0)$ and $\mathbf{a_2} = (0,1)$. Equation 35 has a C_4-symmetry, that is:

$$\hat{C}_4 h_1^{(4)}(k_x, k_y) \hat{C}_4^{-1} = h_1^{(4)}(k_y, -k_x), \tag{36}$$

where $\hat{C}_4$ is given by Eq. (30). Figure 5(b) shows the spectrum of $h_1^{(4)}(\mathbf{k})$ for $t_1 = 1/2$ and $t_2 = 0$, which is gapped at 1/4- and 3/4-filling. For this parameter choice, we have $[X_1^{(2)}] = -1$, $[M_1^{(4)}] = 1$, $[M_2^{(4)}] = 0$, hence $\chi^{(4)} = (-1, 1, 0)$, which corresponds to $\mathbf{P}^{(4)} = e(\mathbf{a_1} + \mathbf{a_2})/2$. The spectrum closes its gap for $|t_1| + |t_2| = 1$, which occurs simultaneously at the **X** and **Y** point, owing to the C_4-symmetry. For finite t_2, the system remains gapless till $|t_1| = 1 + |t_2|$. At this point, the system becomes gapped once again with $\chi^{(4)} = (0, 0, 0)$, corresponding to $\mathbf{P}^{(4)} = \mathbf{0}$. This behavior, together with the corresponding symmetry indicators $\chi^{(4)}$, is depicted in Fig. 5(c). A third primitive generator for C_2 is obtained by letting the hoppings in the $x-$ and $y-$dirrection be different. In that case, the C_4-symmetry in Fig. 5(a) gets broken into a C_2 symmetry given by

$$\mathcal{I} h_1^{(4)}(k_x, k_y) \mathcal{I}^{-1} = h_1^{(4)}(-k_x, -k_y), \tag{37}$$

where $\mathcal{I} \equiv \hat{C}_4^2$.

Geometric breathing square-octagon. The second generator for C_4 is given by the Bloch-Hamiltonian

$$h_2^{(4)}(\mathbf{k}) = \begin{pmatrix} 0 & t_1 & t_2 + e^{ik_x} & t_1 \\ t_1 & 0 & t_1 & t_2 + e^{ik_y} \\ t_2 + e^{-ik_x} & t_1 & 0 & t_1 \\ t_1 & t_2 + e^{-ik_y} & t_1 & 0 \end{pmatrix}. \tag{38}$$

The underlying system is obtained by inserting the unit cell of Fig. 5(d) into a lattice to form the structure shown in Fig. 5(k). The internal structure of the unit cell is rotated with regard to $h_1^{(4)}(\mathbf{k})$. If the next-nearest-neighbour hopping is set to zero, this lattice represents (breathing) T-Graphene; otherwise, we call it the square-octagon lattice. The lattice has attracted much attention recently, with results ranging from topological phases to flat-band superconductivity [33–35]. The spectrum is gapped for $|t_1| + |t_2| < 1$ at half filling, accompanied with rotation invariants $\chi^{(4)} = (1, 1, -1)$ and $\mathbf{P}^{(4)} = e(\mathbf{a_1} + \mathbf{a_2})/2$. An example of the spectrum for $t_1 = 0$ and $t_2 = 1/2$ is shown in Fig. 5(e). When $|t_1| + |t_2| = 1$, the gap generally closes at the **M** point. However, when $t_1 = 0$ (and therefore $|t_2| = 1$), it closes at both the **M** and **Γ** points. Moreover, when $t_2 = 0$ ($|t_1| = 1$), the gap closes over the full **XM** and **YM** lines in the Brillouin zone. For $|t_2| > 1 + |t_1|$, a new gap opens at the **M** point (if $|t_1| = 0$, this gap opens along the whole **XM** and **YM** lines). This gap is trivial and characterized by $\chi^{(4)} = (0, 0, 0)$, $\mathbf{P}^{(4)} = \mathbf{0}$. For other parameter choices, the system is gapless, as shown in Fig. 5(f).

Geometric stacked breathing square-octagon. Finally, the third C_4-symmetric generator is governed by the Hamiltonian

$$h_3^{(4)}(\mathbf{k}) = \begin{pmatrix} 0 & t_1 & t_2 & t_1 \\ t_1 & 0 & t_1 & t_2 \\ t_2 & t_1 & 0 & t_1 \\ t_1 & t_2 & t_1 & 0 \end{pmatrix} + \begin{pmatrix} 0 & 0 & e^{i(k_x+k_y)} & 0 \\ 0 & 0 & 0 & e^{-i(k_x-k_y)} \\ e^{-i(k_x+k_y)} & 0 & 0 & 0 \\ 0 & e^{i(k_x-k_y)} & 0 & 0 \end{pmatrix}. \tag{39}$$

The underlying system is obtained by inserting the unit cell of Fig. 5(g) into a lattice to form the structure in Fig. 5(l). The system has the same internal structure as $h_1^{(4)}(\mathbf{k})$, as can be seen in Fig. 5(a), but has different intercell hopping. The lattice is formed by overlapping two breathing square-octagon lattices. The spectrum of $h_3^{(4)}(\mathbf{k})$ [Fig. 5(h)] is gapped at half filling for $|t_1| + |t_2| < 1$, characterized by the rotation invariants $\chi^{(4)} = (2, 0, 0)$. This corresponds to $\mathbf{P}^{(4)} = \mathbf{0}$. For $|t_1| + |t_2| = 1$, the gap closes at the $\mathbf{X}$ and $\mathbf{Y}$ points (if $t_1 = 0$, it also closes at the $\mathbf{\Gamma}$ and $\mathbf{M}$ points). For $|t_2| > 1 + |t_1|$, a trivial gap opens at the $\mathbf{\Gamma}$ and $\mathbf{M}$ points with $\chi^{(4)} = (0, 0, 0)$, $\mathbf{P}^{(4)} = \mathbf{0}$. For other values of t_1 and t_2, the system is gapless, as shown in Fig. 5(i).

Latent C_4-symmetric structures. The latent C_4-symmetric cell in Fig. 3(c) can be inserted in the three different lattice structures of Fig. 5(j), Fig. 5(k), or Fig. 5(l). This yields systems with Bloch-Hamiltonians of the form

$$h_{L,i}^{(4)}(\mathbf{k}) = H_L^{(4)} + \begin{pmatrix} \tilde{h}_i^{(4)}(\mathbf{k}) & \emptyset_{4\times9} \\ \emptyset_{9\times4} & \emptyset_{9\times9} \end{pmatrix}. \tag{40}$$

Here $\tilde{h}_i^{(4)}(\mathbf{k})$ are the Hamiltonians given in Eq. (35), Eq. (38), and Eq. (39) with all intracell hoppings set to zero, i.e. only intercell hopping. This is because the second term is only there to connect the latently symmetric cells on a lattice.

For all $h_{L,i}^{(4)}(\mathbf{k})$, we set $t_1 = t_2 = t_0$. Consequently, the Hamiltonians have a geometric C_4-symmetry for $t_3 = 0$. For finite values of t_3, the geometric C_4 symmetry of $h_{L,i}^{(4)}(\mathbf{k})$ gets broken. Nevertheless, the latent symmetry of the unit cell is inherited, which becomes clear upon taking the ISR to the red sites

$$\mathfrak{h}_{L,i}^{(4)}(\mathbf{k}) = h_i^{(4)}\left(\mathbf{k}, t_1 = v_0^{(4)}, t_2 = v_1^{(4)}\right) + a^{(4)}\mathbb{I}, \tag{41}$$

which commutes with $\hat{C}_4$ given in Eq. (30). The parameters $a^{(4)}$, $v_0^{(4)}$ and $v_1^{(4)}$ are polynomials of a degree larger than 5 [See Appendix B.1]. Consequently, it is not possible to analytically resolve the gap closing conditions as outlined at the end of Sec. 2. Figure 5(n) shows the spectrum of $h_{L,1}^{(4)}(\mathbf{k})$ for $t_0 = t_1 = t_2 = 1$ and $t_3 = 1/2$. The spectrum is gapped at multiple fillings. For simplicity we consider a single filled band. Figure 5(o) shows the numerically obtained phase diagram of $h_{L,1}^{(4)}(\mathbf{k})$ for a single filled band for $t_1 = t_2 = t_0$. The rotation invariants $\chi^{(4)}$ are depicted for the gapped phases. Similarly, the spectrum of $h_{L,2}^{(4)}(\mathbf{k})$ for $t_0 = t_1 = t_2 = -1$ and $t_3 = 0$ is shown in Fig. 5(q). The corresponding phase diagram for 2 filled bands is shown in Fig. 5(r). Finally, Fig. 5(t) shows the spectrum of $h_{L,3}^{(4)}(\mathbf{k})$ for $t_0 = t_1 = t_2 = 1/2$ and $t_3 = 1$. The phase diagram shown in Fig. 5(u) is (numerically) obtained for 3 filled bands. The rotation invariants $\chi^{(4)}$ are depicted for the gapped phases. The topological and trivial phases are represented by the red and blue regions, respectively. The white regions denote metallic gapless states.

4.3.3 C_3-symmetry

For C_3-symmetry, we consider two lattice strucures, namely a "breathing kagome" and a "bearded breathing kagome".
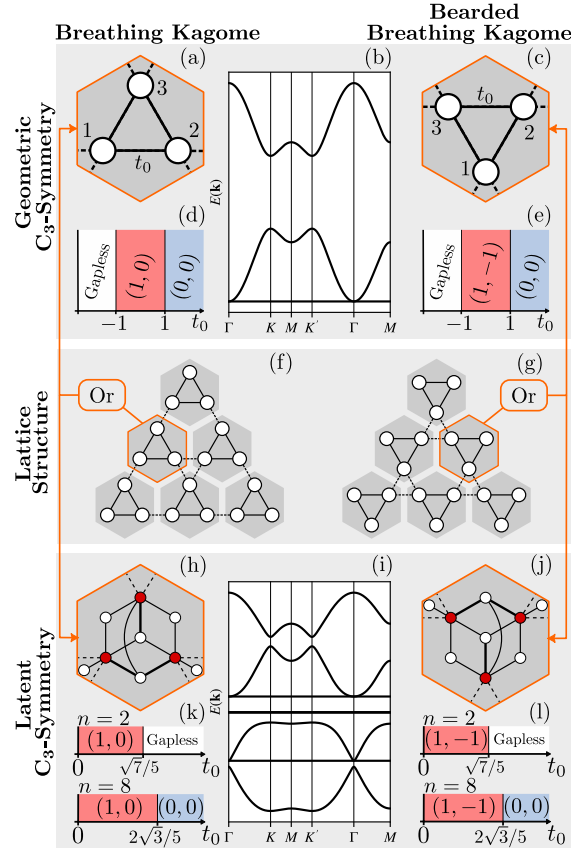
Figure 6: (a,c) Unit cells of the geometric C_3-symmetric primitive generators $h_1^{(3)}(\mathbf{k})$ and $h_2^{(3)}(\mathbf{k})$, respectively. Intracell hopping (black line) has a strength of t_0, while intercell hopping (dashed lines) is fixed to 1. (b) Spectrum of $h_1^{(3)}(\mathbf{k})$ and $h_2^{(3)}(\mathbf{k})$ at $t_0 = 1/2$. (d,e) Phase diagrams of $h_1^{(3)}(\mathbf{k})$ and $h_2^{(3)}(\mathbf{k})$ at 2/3-filling. Rotation invariants $\chi^{(3)}$ are indicated for the gapped phases. (f,g) Lattice structures of the C_3--symmetric primitive generators. The lattices represent a breathing kagome and a bearded breathing kagome lattice, respectively. (h,j) Unit cells of the latent C_3-symmetric primitive generators $h_{L,1}^{(3)}(\mathbf{k})$ and $h_{L,2}^{(3)}(\mathbf{k})$, respectively. Values of the hopping parameters are indicated in Fig. 3(b) and intercell hoppings (dashed lines) are fixed to 1. (i) Spectrum of $h_{L,1}^{(3)}(\mathbf{k})$ and $h_{L,2}^{(3)}(\mathbf{k})$ for $t_0 = 0.6$. (k,l) Phase diagrams at filling $n = 2$ and $n = 8$ for $h_{L,1}^{(3)}$ and $h_{L,2}^{(3)}$, respectively. The rotation invariants $\chi^{(3)}$ are indicated in the different gapped phases.

Geometric C_3-symmetric structures. The internal structure of our geometrically C_3-symmetric unit cells are shown in Figs. 6(a) and (c). They consist of 3 sites connected with an intracell hopping t_0 and an intercell hopping fixed to 1. The two lattice structures for C_3 symmetry are presented in Figs. 6(f)-(g). Since the resulting systems correspond to different terminations of the same Kagome lattice, we will treat them together. The Hamiltonian corresponding to the unit cell shown in Fig. 6(a) inserted into a lattice to form the structure in Fig. 6(f) is given by

$$h_1^{(3)}(\mathbf{k}) = \begin{pmatrix} 0 & t_0 + e^{i\mathbf{k}\cdot\mathbf{a_1}} & t_0 + e^{i\mathbf{k}\cdot\mathbf{a_2}} \\ t_0 + e^{-i\mathbf{k}\cdot\mathbf{a_1}} & 0 & t_0 + e^{-i\mathbf{k}\cdot\mathbf{a_3}} \\ t_0 + e^{-i\mathbf{k}\cdot\mathbf{a_2}} & t_0 + e^{i\mathbf{k}\cdot\mathbf{a_3}} & 0 \end{pmatrix}, \tag{42}$$

while the Bloch-Hamiltonian corresponding to the unit cell in Fig. 6(c), which forms the lattice structure in Fig. 6(g), is given by

$$h_2^{(3)}(\mathbf{k}) = \begin{pmatrix} 0 & t_0 + e^{i\mathbf{k}\cdot\mathbf{a_2}} & t_0 + e^{-i\mathbf{k}\cdot\mathbf{a_3}} \\ t_0 + e^{-i\mathbf{k}\cdot\mathbf{a_2}} & 0 & t_0 + e^{-i\mathbf{k}\cdot\mathbf{a_1}} \\ t_0 + e^{i\mathbf{k}\cdot\mathbf{a_3}} & t_0 + e^{i\mathbf{k}\cdot\mathbf{a_1}} & 0 \end{pmatrix}. \tag{43}$$

The lattice vectors are defined through $\mathbf{a_1} = (1,0)$, $\mathbf{a_2} = (1/2, \sqrt{3}/2)$, and $\mathbf{a_3} = \mathbf{a_1} - \mathbf{a_2}$. $h_1^{(3)}(\mathbf{k})$ and $h_2^{(3)}(\mathbf{k})$ represent a (bearded) breathing Kagome lattice [36–38] which exhibits a C_3 symmetry of the form

$$\hat{C}_3 h_i^{(3)}(k_x, k_y)\hat{C}_3^{-1} = h_i^{(3)}(D_{C_3}\mathbf{k}), \tag{44}$$

with $D_{C_3}\mathbf{k} = \left(-k_x - \sqrt{3}k_y, -k_y + \sqrt{3}k_x\right)/2$ and

$$\hat{C}_3 = \begin{pmatrix} 0 & 0 & 1 \\ 1 & 0 & 0 \\ 0 & 1 & 0 \end{pmatrix}. \tag{45}$$

The spectrum for both Hamiltonians is shown in Fig. 6(b) for $t_0 = 1/2$. For $|t_0| < 1$, the spectrum of $h_1^{(3)}(\mathbf{k})$ [$h_2^{(3)}(\mathbf{k})$] is gapped at 2/3 filling and is described by a topological invariant $\chi^{(3)} = (1,0)$ [$\chi^{(3)} = (1,-1)$] with $\mathbf{P}^{(3)} = (2e/3)(\mathbf{a_1} + \mathbf{a_2})$ [$\mathbf{P}^{(3)} = (e/3)(\mathbf{a_1} + \mathbf{a_2})$]. At $t_0 = 1$, the gap closes at $\mathbf{K}$ and $\mathbf{K}'$ and opens again in a trivial phase with $\chi^{(3)} = (0,0)$ and $\mathbf{P}^{(3)} = \mathbf{0}$ for $t_0 > 1$. At $t_0 = -1$, the gap closes at $\mathbf{\Gamma}$ and the spectrum remains gapless for $t_0 < -1$. The phase diagrams of $h_1^{(3)}(\mathbf{k})$ and $h_2^{(3)}(\mathbf{k})$ are shown in Figs. 6(d) and (e), respectively.

Latent C_3-symmetric structures. Inserting the latently C_3-symmetric unit cell Fig. 3(b) into a lattice to form the structures in Figs. 6(f) and (g) yields two latent C_3-symmetric primitive generators with Bloch-Hamiltonians

$$h_{L,i}^{(3)}(\mathbf{k}) = H_L^{(3)} + \begin{pmatrix} \tilde{h}_i^{(3)}(\mathbf{k}) & \emptyset_{3\times6} \\ \emptyset_{6\times3} & \emptyset_{6\times6} \end{pmatrix}, \tag{46}$$

with $i = 1, 2$. $\tilde{h}_i^{(3)}(\mathbf{k})$ are the Hamiltonians given in Eq. (42) and Eq. (43) with all intracell hoppings set to zero, i.e. only intercell hopping (once again, just to connect the larger cells on a lattice). Figures 6(f) and (g) show lattices corresponding to $h_{L,1}^{(3)}$ and $h_{L,2}^{(3)}$, respectively. Analogous to the non-latent primitive generators for C_3 symmetry, $h_{L,1}^{(3)}$ and $h_{L,2}^{(3)}$ share the same spectrum, as depicted in Fig. 6(i).

The ISR of $h_{L,i}^{(3)}(\mathbf{k})$ to the red sites is given by

$$\mathfrak{h}_{L,i}^{(3)}(\mathbf{k}) = h_i^{(3)}\left(\mathbf{k}, t_0 = v_0^{(3)}\right) + a^{(3)}\mathbb{I}. \tag{47}$$

Owing to the simplicity of the parameters $v_0^{(3)}$ ($= 5t_0^2/E$) and $a^{(3)}$ ($= 7t_0^2/E$), it is possible to analytically derive the phase diagram of this model. In Sec. 4 we showed that $h_i^{(3)}(\mathbf{k})$ has a gap closing at $E = 1$ for $t_0 = 1$, and at $E = 0$ for $t_0 = -1$. Therefore, we obtain the energies E_1^* and E_2^* at which the latent models have a gap closing

$$E_1^* - a^{(3)}(E_1^*) = 1, \quad \text{and} \quad E_2^* - a^{(3)}(E_2^*) = 0. \tag{48}$$

Solving the above equations yields

$$E_1^* = \frac{1}{2}\left(1 \pm \sqrt{1 + 28t_0^2}\right), \quad \text{and} \quad E_2^* = \pm\sqrt{7}t_0. \tag{49}$$

From Eq. (49), we extract the phase transitions through $\nu_0^{(3)}(E_1^*) = 1$ and $\nu_0^{(3)}(E_2^*) = -1$, resulting in

$$t_0 = \pm\frac{2\sqrt{3}}{5}, \pm\frac{\sqrt{7}}{5}. \tag{50}$$

The gap closing energies correspond to a filling of $n = 2$ and $n = 8$ bands out of 9. Using the above derived constraints, we obtain the phase diagrams depicted in Figs. 6(k) and (l) for $h_{L,1}^{(3)}(\mathbf{k})$ and $h_{L,2}^{(3)}(\mathbf{k})$, respectively. The rotation invariants $\chi^{(3)}$ are shown for the different phases. The invariants are the same as those obtained for $h_i^{(3)}(\mathbf{k})$.

4.3.4 C_6-symmetry

For C_6-symmetry, we consider two lattice structures, namely, the "breathing ruby lattice", and the "Kekulé" structure.

Geometric breathing ruby lattice The Hamiltonian for the first C_6-symmetric primitive generator is given by

$$h_1^{(6)}(\mathbf{k}) = \begin{pmatrix} 0 & t_0 & t_1 & t_2 & t_1 & t_0 \\ t_0 & 0 & t_0 & t_1 & t_2 & t_1 \\ t_1 & t_0 & 0 & t_0 & t_1 & t_2 \\ t_2 & t_1 & t_0 & 0 & t_0 & t_1 \\ t_1 & t_2 & t_1 & t_0 & 0 & t_0 \\ t_0 & t_1 & t_2 & t_1 & t_0 & 0 \end{pmatrix} + \begin{pmatrix} 0 & 0 & e^{-i\mathbf{k}\cdot\mathbf{a}_2} & 0 & e^{i\mathbf{k}\cdot\mathbf{a}_3} & 0 \\ 0 & 0 & 0 & e^{i\mathbf{k}\cdot\mathbf{a}_3} & 0 & e^{i\mathbf{k}\cdot\mathbf{a}_1} \\ e^{i\mathbf{k}\cdot\mathbf{a}_2} & 0 & 0 & 0 & e^{i\mathbf{k}\cdot\mathbf{a}_1} & 0 \\ 0 & e^{-i\mathbf{k}\cdot\mathbf{a}_3} & 0 & 0 & 0 & e^{i\mathbf{k}\cdot\mathbf{a}_2} \\ e^{-i\mathbf{k}\cdot\mathbf{a}_3} & 0 & e^{-i\mathbf{k}\cdot\mathbf{a}_1} & 0 & 0 & 0 \\ 0 & e^{-i\mathbf{k}\cdot\mathbf{a}_1} & 0 & e^{-i\mathbf{k}\cdot\mathbf{a}_2} & 0 & 0 \end{pmatrix}. \tag{51}$$

It is obtained by inserting the unit cell from Fig. 7(a) into a lattice to obtain the structure in Fig. 7(g). This lattice is a breathing version of a Ruby lattice. The lattice vectors are given by $\mathbf{a}_1 = (1,0)$, $\mathbf{a}_2 = (1/2, \sqrt{3}/2)$ and $\mathbf{a}_3 = \mathbf{a}_1 - \mathbf{a}_2$. $h_1^{(6)}(\mathbf{k})$ exhibits a C_6 symmetry given by

$$\hat{C}_6 h_1^{(6)}(k_x, k_y)\hat{C}_6^{-1} = h_1^{(6)}(D_{C_6}\mathbf{k}), \tag{52}$$

with $D_{C_6}\mathbf{k} = (k_x - \sqrt{3}k_y, +\sqrt{3}k_x + ky)/2$ and

$$\hat{C}_6 = \begin{pmatrix} 0 & 0 & 0 & 0 & 0 & 1 \\ 1 & 0 & 0 & 0 & 0 & 0 \\ 0 & 1 & 0 & 0 & 0 & 0 \\ 0 & 0 & 1 & 0 & 0 & 0 \\ 0 & 0 & 0 & 1 & 0 & 0 \\ 0 & 0 & 0 & 0 & 1 & 0 \end{pmatrix}. \tag{53}$$

First, consider the case $t_1 = t_2 = 0$. The spectrum is gapped at 2/3-filling if $|t_0| < 1$. The gap is characterised by $\chi^{(6)} = (0, 2)$, which corresponds to $\mathbf{P}^{(6)} = \mathbf{0}$ and $Q^{(6)} = e/3$. This can be seen in the spectrum in Fig. 7(b), which is calculated for $t_0 = 1/2$. At $t_0 = 1$, the gap closes at the $\mathbf{\Gamma}$ point and upon further increase of t_0, the spectrum remains gapless. If we only impose $t_2 = 0$, the phase diagram in Fig. 7(c) is obtained. For values of t_0 and t_1 in the red region, the system is in a topological phase with $\chi^{(6)} = (0, 2)$. Leaving the topological phase (red) by increasing t_1, the gap closes at the $\mathbf{K}$ and $\mathbf{K}'$ points and the spectrum is gapless. Upon further increasing t_1, a trivial gap $[\chi^{(6)} = (0, 0)]$ reopens at the $\mathbf{K}$ and $\mathbf{K}'$ points.

Geometric Kekulé The Hamiltonian for the second C_6-symmetric primitive generator is given by

$$
h_2^{(6)}(\mathbf{k}) = \begin{pmatrix} 0 & t_0 & t_1 & t_2 & t_1 & t_0 \\ t_0 & 0 & t_0 & t_1 & t_2 & t_1 \\ t_1 & t_0 & 0 & t_0 & t_1 & t_2 \\ t_2 & t_1 & t_0 & 0 & t_0 & t_1 \\ t_1 & t_2 & t_1 & t_0 & 0 & t_0 \\ t_0 & t_1 & t_2 & t_1 & t_0 & 0 \end{pmatrix} + \begin{pmatrix} 0 & 0 & 0 & e^{-i\mathbf{k}\cdot\mathbf{a}_2} & 0 & 0 \\ 0 & 0 & 0 & 0 & e^{i\mathbf{k}\cdot\mathbf{a}_3} & 0 \\ 0 & 0 & 0 & 0 & 0 & e^{i\mathbf{k}\cdot\mathbf{a}_1} \\ e^{i\mathbf{k}\cdot\mathbf{a}_2} & 0 & 0 & 0 & 0 & 0 \\ 0 & e^{-i\mathbf{k}\cdot\mathbf{a}_3} & 0 & 0 & 0 & 0 \\ 0 & 0 & e^{-i\mathbf{k}\cdot\mathbf{a}_1} & 0 & 0 & 0 \end{pmatrix}. \tag{54}
$$

The corresponding system is obtained by using the unit cell of Fig. 7(d) to form the lattice structure in Fig. 7(h). Note that it has the same unit cell as in the Breathing Ruby Lattice case, but rotated and with different intercell hopping. The lattice vectors $\mathbf{a}_1$, $\mathbf{a}_2$, and $\mathbf{a}_3$ are the same as in the breathing ruby lattice case. We note that the different intercell hopping structure forms a breathing honeycomb or Kekulé lattice [39, 40]. Just as Eq. (51), the primitive generator Eq. (54) has a C_6 symmetry given by Eq. (52). Again, first consider $t_1 = t_2 = 0$. The spectrum is gapped at 1/2-filling for $-1/2 < t_0 < 1$, as shown in Fig. 7(e), where $t_0 = 1/2$. This gap is characterised by $\chi^{(6)} = (2,0)$, which corresponds to $\mathbf{P}^{(6)} = \mathbf{0}$ and $Q^{(6)} = e/2$. For fixed $t_2 = 0$, the phase diagram in Fig. 7(f) is obtained. The system is in its topological phase $[\chi^{(6)} = (2,0)]$ for $-1/2 < t_0 < 1$ and $|t_1| < (t_0 + 2)/3$. At $t_0 = 1$ or $|t_1| = (t_0 + 2)/3$, the gap closes at the Γ point. For $t_0 > 1$ and $|t_1| < |t_0|$, the gap reopens in a trivial phase with $\chi^{(6)} = (0,0)$.

Latent C_6-symmetric structures. The latent primitive generators for C_6-symmetry are given by

$$
h_{L,i}^{(6)}(\mathbf{k}) = H_L^{(6)} + \begin{pmatrix} \tilde{h}_i^{(6)}(\mathbf{k}) & \emptyset_{6\times 13} \\ \emptyset_{13\times 6} & \emptyset_{13\times 13} \end{pmatrix}. \tag{55}
$$

Here, $\tilde{h}_i^{(6)}(\mathbf{k})$ are the Hamiltonians given in Eq. (51), Eq. (54) with all intracell hoppings set to zero, i.e. only intercell hopping (to connect the large unit cells on a lattice). The two systems corresponding to $h_{L,1}^{(6)}(\mathbf{k})$ and $h_{L,2}^{(6)}(\mathbf{k})$ are obtained by inserting the latently C_6-symmetric unit cell shown in Fig. 3(d) into a lattice structure to form Fig. 7(g) and Fig. 7(h), respectively. The intercell hopping (dashed) is fixed to 1. The ISR of $\mathfrak{h}_{L,i}^{(6)}(\mathbf{k})$ is given by

$$
\mathfrak{h}_{L,i}^{(6)}(\mathbf{k}) = h_i^{(6)}\left(\mathbf{k}, t_0 = v_0^{(6)}, t_1 = v_1^{(6)}, t_2 = v_2^{(6)}\right) + a^{(6)}\mathbb{I}, \tag{56}
$$

which is symmetric under the action of $\hat{C}_6$, i.e. Eq. (52). Since the parameters $a^{(6)}$ and $v_i^{(6)}$ are ratios of large order polynomials in E, it is not possible to analytically obtain the phase diagrams of $h_{L,i}^{(6)}(\mathbf{k})$. Figure 7(j) [Fig. 7(m)] show the spectrum of $h_{L,1}^{(6)}(\mathbf{k})$ [$h_{L,2}^{(6)}(\mathbf{k})$] for $t_0 = t_1 = t_2 = 1/4$. A phase diagram of $h_{L,1}^{(6)}(\mathbf{k})$ for 4 filled bands is shown in Fig. 7(k), revealing a topological phase characterised by $\chi^{(6)} = (0,2)$ separated by a gapless phase from the trivial phase $\chi^{(6)} = (0,0)$. Moreover, Fig. 7(n) shows a phase diagram of $h_{L,2}^{(6)}(\mathbf{k})$ for 3 filled bands. Both phase diagrams reveal the presence of the same topological phases as in $h_i^{(6)}(\mathbf{k})$.

We once more emphasize that the presence of a hidden (latent) symmetry in the lattices protects these higher-order topological phases. Since these latent symmetries behave much like their geometric counterparts, they also give rise to very similar topological phases.

5 Construction of latent HOTIs

We are now finally equipped with all the necessary tools to allow an efficient design of latent HOTIs.
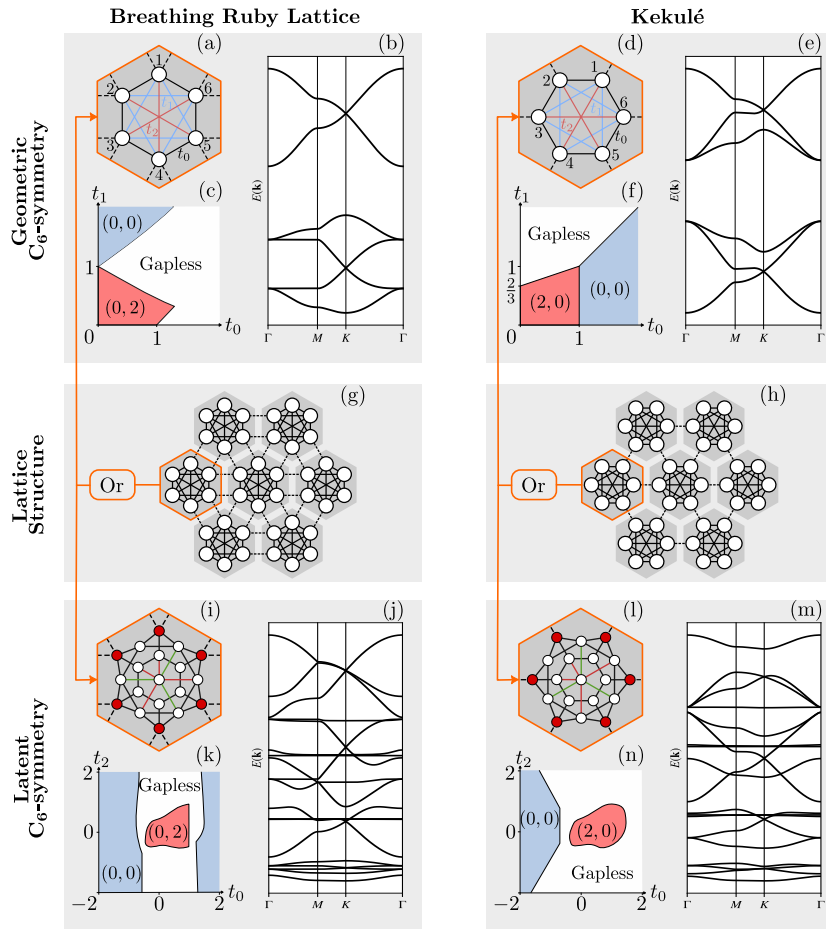
Figure 7: (a,d) Unit cells of the geometric C_6-symmetric primitive generators $h_1^{(6)}(\mathbf{k})$ and $h_2^{(6)}(\mathbf{k})$. Three C_6 preserving hoppings t_0 (black), t_1 (blue) and t_2 (red) are indicated. Intercell hopping (dashed) is fixed to 1. (b,e) Spectra of $h_1^{(6)}(\mathbf{k})$ and $h_2^{(6)}(\mathbf{k})$, for $t_0 = 1/2$, $t_1 = t_2 = 0$. (c,f) Phase diagrams of $h_1^{(6)}(\mathbf{k})$, and $h_2^{(6)}(\mathbf{k})$ in the $t_0 - t_1$ plane with $t_2 = 0$. Rotation invariants $\chi^{(6)}$ are indicated for gapped phases. (g,h) Lattice structures of the C_6-symmetric primitive generators. The lattices represent a breathing ruby lattice and a kekulé lattice, respectively. (i,l) Unit cells of the latent C_6-symmetric primitive generators $h_{L,1}^{(6)}(\mathbf{k})$ and $h_{L,2}^{(6)}(\mathbf{k})$. Values of the hopping parameters are indicated in Fig. 3(d) and intercell hoppings (dashed lines) are fixed to 1. (j,m) Spectra of $h_{L,1}^{(6)}(\mathbf{k})$ and $h_{L,2}^{(6)}(\mathbf{k})$, for $t_0 = 3/4$, $t_1 = 7/8$, $t_2 = 1/8$. (k,n) Phase diagrams of $h_{L,1}^{(6)}(\mathbf{k})$ for $n = 4$ filled bands and $h_{L,2}^{(6)}(\mathbf{k})$ for $n = 3$ filled bands, with $t_1 = 1/4$. Rotation invariants $\chi^{(6)}$ are indicated in the gapped phases.

As mentioned above, any HOTI (geometric or latent) must fulfill the following two constraints:

- The corner charge $Q^{(n)}$, as given by Eq. (24), is nonzero.

- The dipole moment $\mathbf{P}^{(n)}$, as given by Eq. (23), vanishes.

In the following, we will construct latent HOTIs featuring a C_n symmetry. Although there are many possibilities, for brevity, we only show a single example of C_3-, C_4-, and C_6-symmetry
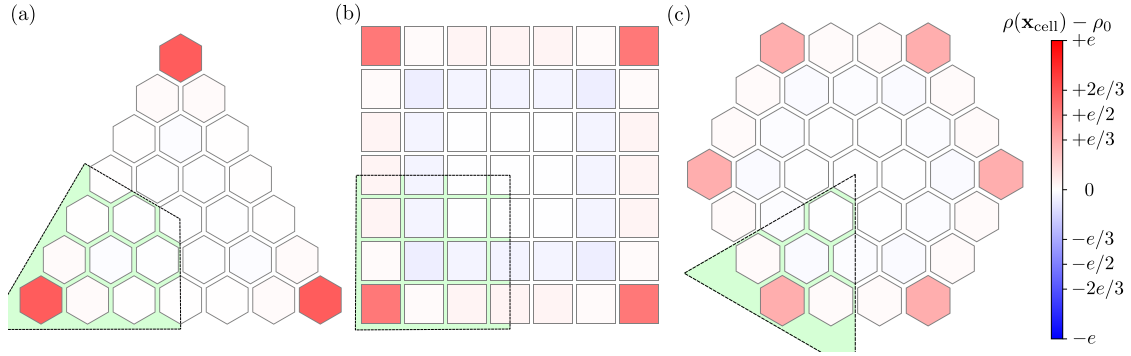
Figure 8: Latent higher-order topological insulators. (a) Triangular OBC flake of $h_L^{(3)}(\mathbf{k})$ for $t_0 = 0.2$ and $g = 0.1$ at filling $N_f = 18N_{\text{cells}} + 2$. Each of the corners shows a quantized excess corner charge of $Q_{\text{corner}} = 2e/3$. (b) Square OBC flake of $h_{L,2}^{(4)}(\mathbf{k})$ for $t_0 = t_1 = t_2 = 1/2$ and $t_3 = 1$ at filling $N_f = 3N_{\text{cells}} + 2$. Each of the corners shows a quantized excess corner charge of $Q_{\text{corner}} = e/2$. (c) Hexagonal OBC flake of $h_{L,1}^{(6)}(\mathbf{k})$ for $t_0 = t_1 = t_2 = 1/4$ at filling $N_f = 17N_{\text{cells}} + 2$. Each of the corners shows a quantized excess corner charge of $Q_{\text{corner}} = e/3$.

each. C_2−symmetry is left out as constructing a lattice with only two 'corners' would correspond to a 1D chain, which is already treated in Ref. [21]. Alternatively, a square latent C_2−symmetric lattice could be considered, which only shows pairwise equal corner charges.

Latent C_3-symmetric HOTI The latent C_3-symmetric generators $h_{L,i}^{(3)}(\mathbf{k})$ have topological phases with $\chi^{(3)} = (0,2)$ and $\chi^{(3)} = (2,0)$, which corresponds to $\mathbf{P}^{(3)} = (e/3)(\mathbf{a_1} + \mathbf{a_2})$ and $\mathbf{P}^{(3)} = (2e/3)(\mathbf{a_1} + \mathbf{a_2})$, respectively. For neither of these models the dipole moment vanishes. In Sec. 4.3 we argued that the generators may be stacked to obtain models with arbitrary rotational invariant, and, thus arbitrary $\mathbf{P}^{(n)}$ and $Q^{(n)}$. By 'stacking' $h_{L,1}^{(3)}(\mathbf{k})$ and $h_{L,2}^{(3)}(\mathbf{k})$, we obtain

$$h_L^{(3)}(\mathbf{k}) = \begin{pmatrix} h_{L,1}^{(3)}(\mathbf{k}) & \mathcal{T} \\ \mathcal{T}^\dagger & h_{L,2}^{(3)}(\mathbf{k}) \end{pmatrix}, \tag{57}$$

where $\mathcal{T}$ couples the two models without breaking C_3-symmetry and without closing the gap. Here, we choose

$$\mathcal{T} = \begin{pmatrix} T & \emptyset_{3\times 6} \\ \emptyset_{6\times 3} & \emptyset_{6\times 6} \end{pmatrix}, \qquad T = \begin{pmatrix} g & 0 & g \\ g & g & 0 \\ 0 & g & g \end{pmatrix}. \tag{58}$$

From Fig. 6, we observe that both $h_{L,i}^{(3)}(\mathbf{k})$ are topological for $t_0 = 0.2$ at 8 filled bands. Taking $g = 0.1$ does not close the gap, such that $h_L^{(3)}(\mathbf{k})$ is characterised by $\chi^{(3)} = (0,2) + (2,0) = (2,2)$. This translates to $\mathbf{P}^{(3)} = \mathbf{0}$ and $Q^{(3)} = 2e/3$. Figure 8(a) shows a triangular flake with OBC corresponding to $h_L^{(3)}(\mathbf{k})$, in which every hexagon represents a (stacked) unit cell. The colour of the cells represents $\rho(\mathbf{x}_{\text{cell}}) - \rho_0$ where

$$\rho(\mathbf{x}_{\text{cell}}) = e \sum_{\mathbf{x} \in \mathbf{x}_{\text{cell}}} \sum_i^{N_f} |\psi_i(\mathbf{x})|^2, \tag{59}$$

is the electronic charge density per unit cell and N_f is the amount of filled states. $\psi_i(\mathbf{x})$ is the wavefunction of the ith energy eigenstate of the electron. ρ_0 is the (ionic) background charge density of the unit cells ($\rho_0 = e \times$ #filled bands $\times$ #cells). In Fig. 8(a), we take a filling of 16

bands (8 filled bands of each model). There is a clear localisation of excess charge in the three corners of the flake. Adding up the excess charge within a single sector (indicated in green), reveals that the corner charge is quantized and equal to $Q_{\text{corner}} = 2e/3$.

Latent C_4-symmetric HOTI As an example of C_4-symmetric latent HOTI, we may take $h_{L,2}^{(4)}(\mathbf{k})$, which in its topological phase $[\chi^{(4)} = (2,0,0)]$ at 3 filled bands has $\mathbf{P}^{(4)} = \mathbf{0}$ and $Q^{(4)} = e/2$, i.e., it is not necessary to stack two models. Figure 8(b) shows the charge density in a square flake with OBC, described by $h_{L,2}^{(4)}(\mathbf{k})$ for $t_0 = t_1 = t_2 = 1/2$ and $t_3 = 1$. Summing over a single sector (green) reveals a total corner charge of $Q_{\text{corner}} = e/2$, predominantly localized at the corners.

Latent C_6-symmetric HOTI Finally, from Eq. (23), it follows that the dipole moment always vanishes for any C_6-symmetric system. Consequently, both primitive generators $h_{L,i}^{(6)}(\mathbf{k})$ will represent a HOTI in their topological phase. Here, we consider $h_{L,1}^{(6)}(\mathbf{k})$ for $t_0 = t_1 = t_2 = 1/4$ for 17 filled bands. For these parameters, the system is gapped and characterised by $\chi^{(6)} = (0,2)$, corresponding to $\mathbf{P}^{(6)} = \mathbf{0}$ and $Q^{(6)} = e/3$. Figure 8(c) shows a hexagonal flake of this system, with OBC. It displays corner charges $Q_{\text{corner}} = e/3$ in each of the six corners of the flake.

In addition to the charge density distributions of the three examples shown in Fig. 8, we further present in Fig. 9 the corner modes in each of the lattices that we treated. In Fig. 8, we displayed the quantized fractional corner charges through the quantity $\rho(\mathbf{x}_{\text{cell}}) - \rho_0$. We now show the states themselves. For a C_n-symmetric system, there are n corner states. In Fig. 9, the size of the blue circles represents the combined amplitude of one set of corner states, i.e.

$$\nu(\mathbf{x}) = \sum_{i=1}^{n} |\psi_i^{\text{corner}}(\mathbf{x})|^2\,, \tag{60}$$

where $n = 2, 3, 4, 6$ for C_2-, C_3-, C_4-, C_6-symmetry, respectively.

A close inspection of the latent C_3- and C_6-symmetric lattices [Figs. 9(d-g)] leads to the conclusion that these states do not have a rotation symmetry. Indeed, this can be explained by the fact that these states are protected by a latent symmetry instead of a conventional symmetry. Moreover, when only considering the support of the wavefunction on the S sites (red sites in the insets), the corner states look indeed symmetric. This is verified by the smaller plot next to Fig. 9(f), which shows the same wavefunction but only on S.

6 Topological robustness

In this section, we further investigate the robustness of the latent higher-order topological phases compared to their conventional counterparts. As a working example, we choose the (latent) breathing Kagome lattice. Before including disorder, we show in Figs. 10(a) and 10(b) show the open boundary spectra of a triangular flake of the geometric and latent breathing Kagome lattice, respectively. The spectrum is plotted as a function of the intercell hopping parameter w, which was previously fixed to 1. The vertical red dashed lines indicate the value of w for which a topological phase transition occurs through a bulk gap closing. The horizontal green dashed lines indicate the presence of a topological corner mode. Notice that in Fig. 10(b), the corner states do not lie at zero energy, and can sometimes be hidden by the bulk-bands.
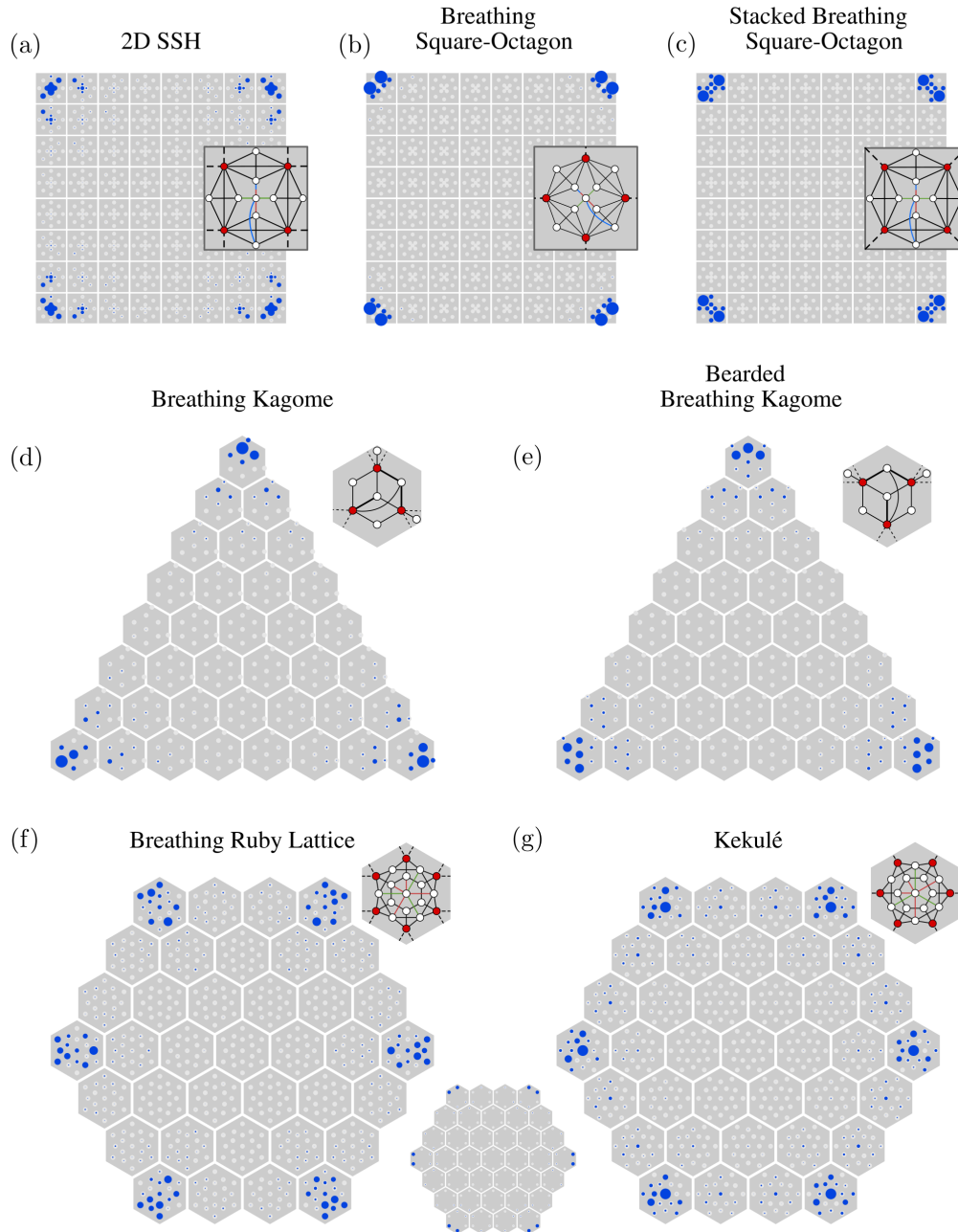
Figure 9: Corner states in the latent lattices considered in Figs. 5, 6, and 7. Blue circles represent the wavefunction amplitude of the corner states as defined through Eq. (60) while grey circles denote the sites in the unit cell. States are calculated for parameters: (a) $t_0 = t_1 = t_2 = 1$, $t_3 = 0.5$, (b) $t_0 = t_1 = t_2 = 0.25$, $t_3 = 0$, (c) $t_0 = t_1 = t_2 = 0.5$, $t_3 = 1$, (d,e) $t_0 = 0.2$, (f,g) $t_0 = t_1 = t_2 = 0.25$.
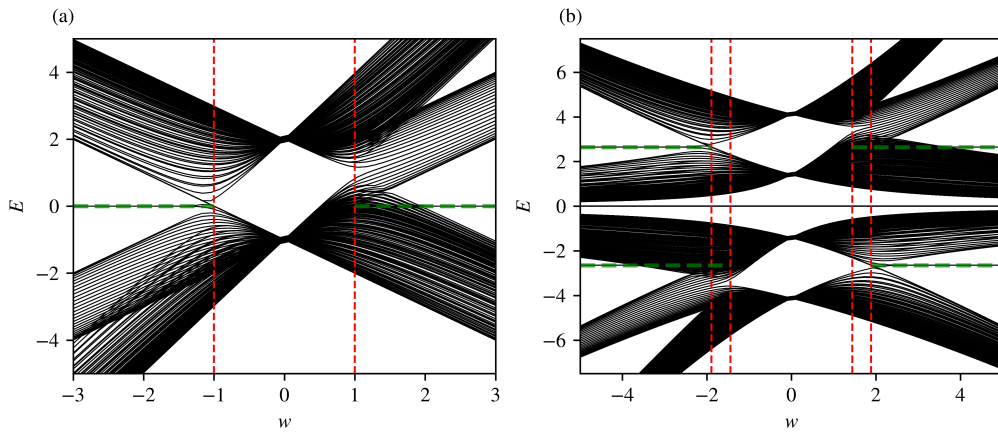
Figure 10: Spectra of (a) the geometric and (b) latent kagome model on a triangular flake geometry as a function of intercell hopping w. Red lines indicate values of w for which a topological phase transition occurs, while green lines mark the topological corner states.

6.1 Onsite disorder

The systems considered in this work are protected by latent/geometric symmetries, which offer weaker protection than spectral symmetries. Consequently, most perturbations break the (latent) C_n symmetries that protect the crystalline topological phases. If the perturbation is sufficiently small, the corner modes may persist, although their degeneracy will be lifted by a small amount. To demonstrate this, we consider random onsite disorder, i.e., a perturbation Hamiltonian of the form

$$H_{\text{disorder}} = \sum_i D_i c_i^\dagger c_i, \tag{61}$$

where the disorder strength D_i is sampled from a uniform distribution $[-D, D]$. Figure 11 shows the spectra and corner-state wavefunctions for an open boundary conditions flake of the geometric and latent kagome model at different disorder strengths D. The introduction of onsite disorder immediately lifts the degeneracy of the corner states. However, if the disorder is sufficiently small, they will still be pinned to the corners. If the disorder strength becomes large enough, in this case at $D \approx 0.6$, the corner states cease to exist, as seen in the right panels of Figs. 11(a) and 11(b).

6.2 Orientational disorder

The latent lattices allow for a type of disorder exclusive to systems with latent symmetries, namely, orientational disorder [21]. It is created by taking the latently symmetric unit cells in a lattice and rotating them by their respective symmetry, as seen in Fig. 12. Since rotating the unit cell does not affect the isospectral reduction of a lattice, a lattice with orientational disorder has the same spectral properties as a lattice with no orientational disorder. Consequently, the behavior of such a lattice is unperturbed.
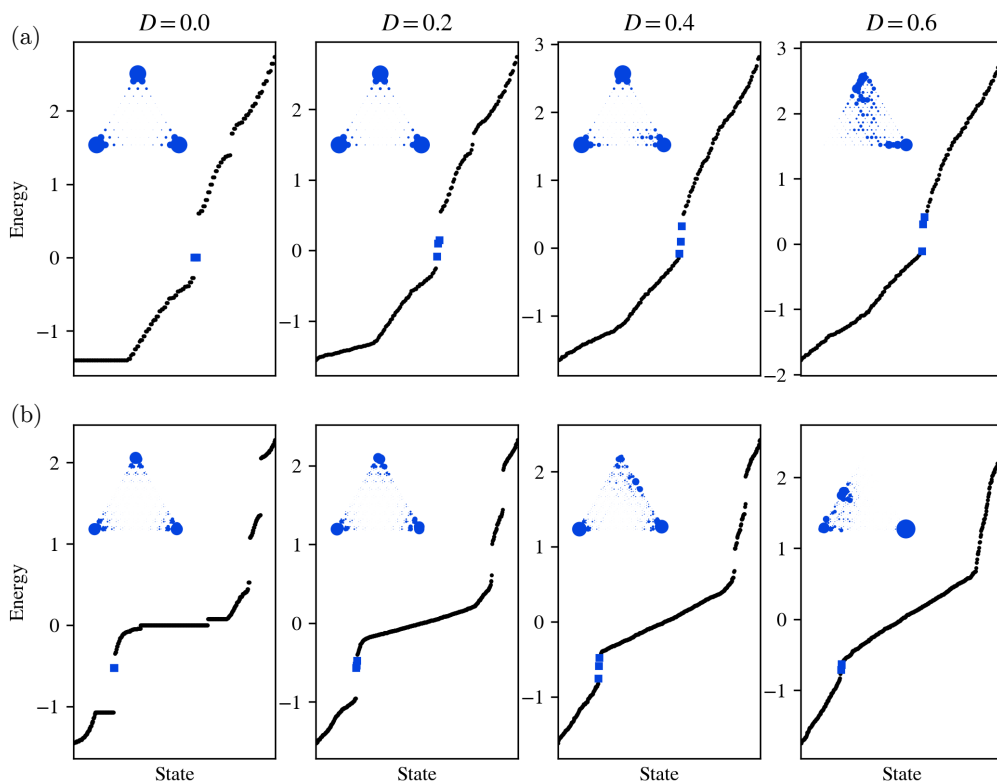
Figure 11: Open boundary condition flake of (a) the geometric Kagome model for $t_0 = 0.4$ and (b) the latent Kagome model for $t_0 = 0.2$, at different disorder strength D. Insets show the (combined) wavefunction amplitudes of the three corner states indicated by the blue squares.
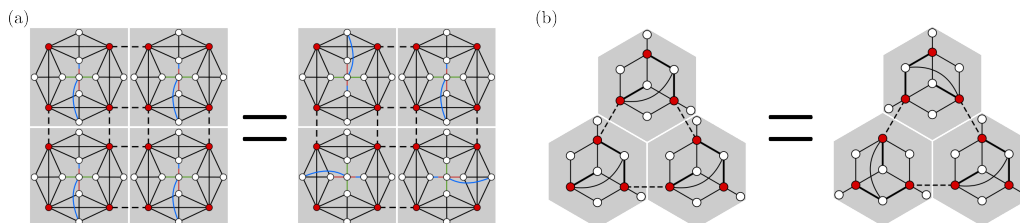
Figure 12: Examples of a latently symmetric lattice with (a) latent C_4 and (b) latent C_6 symmetry together with examples of orientational disorder.

7 Conclusion

In this paper, we have shown that the existence of non-trivial fractional corner charges in two dimensional systems does not require the preservation of a C_n-symmetry. Instead, a latent symmetry is sufficient. This may be understood from the behaviour of the latent symmetry $\hat{C}_n \oplus \overline{Q}^{(n)}$ at the HSPs $\mathbf{\Pi}$, which is exactly the same as for a non-latent symmetry, i.e. $[h(\mathbf{\Pi}), \hat{C}_n \oplus \overline{Q}^{(n)}]_- = 0$. Owing to this property, any two dimensional system with a latent symmetry of the form $\hat{C}_n \oplus \overline{Q}^{(n)}$ may host non-trivial corner modes and can be characterised in terms of rotation invariants. In Section 4 we gave examples of primitive generators that have this property. We showed that for some models, a full analytical treatment is possible, even though the model had up to 9 bands. This reveals another strength of our method: if, under an isospectral reduction, a Hamiltonian reduces to an energy-dependent version of a known

model, then properties of the known model can be used to characterize the full Hamiltonian. A formal outline of this procedure was given at the end of Section 2.

We have given examples of unit cells that show a latent C_n-symmetry for the four rotation symmetries that tile the two-dimensional space and have provided an outline for how to construct latent HOTIs based on these. Nevertheless, our work does not restrict itself to these unit cells. On the contrary, any cell that obeys a latent C_n-symmetry may be used to construct a latent HOTI. These unit cells were used merely to give three specific examples of a latent HOTI. We emphasize that these examples do not capture the full range of possible latent HOTIs. Any two primitive generators based on a unit cell – geometric- or latent symmetric – can be combined to form a new generator. One could obtain HOTIs that are composed of one geometric generator and one latent generator. The examples we have provided – namely, the 2D SSH model, a breathing square-octagon lattice, T-Graphene, a breathing kagome lattice, a breathing ruby lattice, and a Kekulé lattice [30–38, 40] – have all been previously used to study a variety of phenomena, which is why we believe that our results might therefore be directly relevant to them.

In addition, we discussed the possibility of a unit cell showing a geometric C_3 (C_2) symmetry while its ISR showed a latent C_6 (C_4) symmetry, i.e. an effective symmetry doubling. Consequentially, the corner charges will follow the doubled symmetry. This behaviour can neatly be explained by performing an ISR.

Moreover, TCIs protected by C_n-symmetry only form a subset of all crystalline topological phases. Similar methods to those outlined in our work can be applied to systems with different crystalline symmetries. This leads us to believe that our work opens doors for the latent generalisation of topological phases protected by other crystalline symmetries. Interesting cases for future investigations would be latent versions of topological systems lacking translational symmetry, but still displaying global space-group symmetries. Examples of these are possibly a generalization of a recent work on 1D topological quasicrystalline insulators [41], or a crystalline generalization of the topological states observed in finite fractals [42].

Finally, it would be interesting to investigate a generalization to third-order topological insulators in 3D. There is no straightforward 3D generalization of the theory outlined in Ref. [14]. Still, using the same method to construct the unit cells of this work, one could find a unit cell that reduces to a latent version of the one found in the pyrochlore lattice [43], which is known to host a third-order topological phase with quantized fractional charges.

Acknowledgments

A Derivation of the $\overline{Q}$ matrix

Reference [20] gives a derivation for the Q (and therefore also $\overline{Q}$) matrix. Here, we will briefly outline how to construct Q in the specific case of a latent C_n-symmetry. Let H be a real symmetric matrix with a latent C_n-symmetry, i.e.

$$\left[\mathcal{R}_S(H, E), \hat{C}_n \right]_- = 0. \tag{A.1}$$

Then the eigenstates $\{|\phi\rangle\}$ of H can be chosen to satisfy

$$\hat{C}_n |\phi\rangle_S = e^{\frac{2\pi i}{n}(p-1)} |\phi\rangle_S, \quad \text{with} \quad p \in \{1, 2, \ldots, n\}, \qquad \text{OR} \qquad |\phi\rangle_S = \mathbf{0}, \tag{A.2}$$

where $\mathbf{0}$ is a zero vector in the S subspace. We label these states by $\left|\phi^{(p)}\right\rangle$ and $\left|\phi^{(0)}\right\rangle$, respectively. One can then define the projectors

$$P_p = \sum_i \left|\phi_i^{(p)}\right\rangle\left\langle\phi_i^{(p)}\right|, \qquad P_0 = \sum_i \left|\phi_i^{(0)}\right\rangle\left\langle\phi_i^{(0)}\right|. \tag{A.3}$$

From these projectors, Q is defined through

$$Q = \hat{C}_n \oplus \overline{Q} = P_0 + \sum_{p=1}^n e^{\frac{2\pi i}{n}(p-1)} P_p. \tag{A.4}$$

B Hamiltonians and symmetries

B.1 C_4

The Hamiltonian for the unit cell in Fig. 3(c) of the main text is given by

$$H_L^{(4)} = \begin{pmatrix}
0 & 1 & 0 & 1 & 1 & 0 & 0 & 1 & 1 & 0 & 0 & 1 & 0 \\
1 & 0 & 1 & 0 & 1 & 1 & 0 & 0 & 1 & 1 & 0 & 0 & 0 \\
0 & 1 & 0 & 1 & 0 & 1 & 1 & 0 & 0 & 1 & 1 & 0 & 0 \\
1 & 0 & 1 & 0 & 0 & 0 & 1 & 1 & 0 & 0 & 1 & 1 & 0 \\
1 & 1 & 0 & 0 & 0 & 0 & 0 & 0 & 1 & 0 & 0 & 0 & t_1+t_3 \\
0 & 1 & 1 & 0 & 0 & 0 & 0 & 0 & 0 & 1 & 0 & 0 & t_2 \\
0 & 0 & 1 & 1 & 0 & 0 & 0 & 0 & 0 & 0 & 1 & 0 & t_1 \\
1 & 0 & 0 & 1 & 0 & 0 & 0 & 0 & 0 & 0 & 0 & 1 & t_2 \\
1 & 1 & 0 & 0 & 1 & 0 & 0 & 0 & 0 & 0 & 0 & 0 & 0 \\
0 & 1 & 1 & 0 & 0 & 1 & 0 & 0 & 0 & 0 & 0 & 0 & 0 \\
0 & 0 & 1 & 1 & 0 & 0 & 1 & 0 & 0 & 0 & 0 & 0 & t_3 \\
1 & 0 & 0 & 1 & 0 & 0 & 0 & 1 & 0 & 0 & 0 & 0 & 0 \\
0 & 0 & 0 & 0 & t_1+t_3 & t_2 & t_1 & t_2 & 0 & 0 & t_3 & 0 & 0
\end{pmatrix}. \tag{B.1}$$

The symmetry on the level of the full Hamiltonian $H_L^{(4)}$ is given by

$$Q^{(4)} = \hat{C}_4 \oplus \overline{Q}^{(4)} = \begin{pmatrix}
0 & 0 & 0 & 1 \\
1 & 0 & 0 & 0 \\
0 & 1 & 0 & 0 \\
0 & 0 & 1 & 0
\end{pmatrix} \oplus \begin{pmatrix}
\frac{3}{4} & -\frac{1}{4} & \frac{1}{4} & \frac{1}{4} & -\frac{1}{4} & -\frac{1}{4} & \frac{1}{4} & \frac{1}{4} & 0 \\
\frac{1}{4} & \frac{3}{4} & -\frac{1}{4} & \frac{1}{4} & \frac{1}{4} & -\frac{1}{4} & -\frac{1}{4} & \frac{1}{4} & 0 \\
\frac{1}{4} & \frac{1}{4} & \frac{3}{4} & -\frac{1}{4} & \frac{1}{4} & \frac{1}{4} & -\frac{1}{4} & -\frac{1}{4} & 0 \\
-\frac{1}{4} & \frac{1}{4} & \frac{1}{4} & \frac{3}{4} & -\frac{1}{4} & \frac{1}{4} & \frac{1}{4} & -\frac{1}{4} & 0 \\
-\frac{1}{4} & -\frac{1}{4} & \frac{1}{4} & \frac{1}{4} & \frac{3}{4} & -\frac{1}{4} & \frac{1}{4} & \frac{1}{4} & 0 \\
\frac{1}{4} & -\frac{1}{4} & -\frac{1}{4} & \frac{1}{4} & \frac{1}{4} & \frac{3}{4} & -\frac{1}{4} & \frac{1}{4} & 0 \\
\frac{1}{4} & \frac{1}{4} & -\frac{1}{4} & -\frac{1}{4} & \frac{1}{4} & \frac{1}{4} & \frac{3}{4} & -\frac{1}{4} & 0 \\
-\frac{1}{4} & \frac{1}{4} & \frac{1}{4} & -\frac{1}{4} & -\frac{1}{4} & \frac{1}{4} & \frac{1}{4} & \frac{3}{4} & 0 \\
0 & 0 & 0 & 0 & 0 & 0 & 0 & 0 & 1
\end{pmatrix}. \tag{B.2}$$

Figure 13: A more complex latent C_6−symmetric unit cell. The hopping parameters are indicated by different colors.

The reduced parameters that enter Fig. 3(g) and Eq. (41) are given by

$$a^{(4)} = \frac{t_0^2\left(4E\left(E^2 - t_0^2\right) + t_1^2(t_0 - 7E) + 2\left(t_2 - 3t_3\right)t_1(E + t_0) + t_2^2(t_0 - 7E) + t_3^2(t_0 - 7E) + 2t_2t_3(E + t_0)\right)}{(t_0 - E)\left(E(t_0 - E)(E + t_0) + 2\left(Et_1^2 + t_3t_1(E + t_0) + E\left(t_2^2 + t_3^2\right)\right)\right)},$$

(B.3)

$$v_0^{(4)} = -\frac{t_0(E + t_0)\left(t_1^2(-(t_0 - 2E)) + t_1\left(2Et_3 - 2t_0t_2\right) - t_2^2(t_0 - 2E) - t_3^2(t_0 - 2E) + E(t_0 - E)(E + t_0) - 2t_0t_2t_3\right)}{(t_0 - E)\left(E(t_0 - E)(E + t_0) + 2\left(Et_1^2 + t_3t_1(E + t_0) + E\left(t_2^2 + t_3^2\right)\right)\right)},$$

(B.4)

$$v_1^{(4)} = \frac{t_0^2\left(t_1 + t_2 + t_3\right)^2(E + t_0)}{(t_0 - E)\left(E(t_0 - E)(E + t_0) + 2\left(Et_1^2 + t_3t_1(E + t_0) + E\left(t_2^2 + t_3^2\right)\right)\right)}.$$

(B.5)

B.2 C_6

The Hamiltonian for the unit cell in Fig. 3(d) of the main text is a simplified version of the one denoted in Fig. 13. To obtain the former, we set $t_2 = t_3 = t_4 = 0$ and let $t_5 \rightarrow t_2$. The full Hamiltonian is given by

$$H_L^{(6)} = \begin{pmatrix}
0 & 0 & 0 & 0 & 0 & 0 & 0 & 0 & 0 & 0 & t_0 & 0 & 0 & 0 & 0 & t_0 & t_0 & 0 & 0 \\
0 & 0 & 0 & 0 & 0 & 0 & 0 & 0 & 0 & 0 & 0 & t_0 & 0 & 0 & 0 & 0 & t_0 & t_0 & 0 \\
0 & 0 & 0 & 0 & 0 & 0 & t_0 & 0 & 0 & 0 & 0 & 0 & t_0 & 0 & 0 & 0 & 0 & t_0 & 0 \\
0 & 0 & 0 & 0 & 0 & 0 & 0 & t_0 & 0 & 0 & 0 & 0 & t_0 & t_0 & 0 & 0 & 0 & 0 & 0 \\
0 & 0 & 0 & 0 & 0 & 0 & 0 & 0 & t_0 & 0 & 0 & 0 & 0 & t_0 & t_0 & 0 & 0 & 0 & 0 \\
0 & 0 & 0 & 0 & 0 & 0 & 0 & 0 & 0 & t_0 & 0 & 0 & 0 & 0 & t_0 & t_0 & 0 & 0 & 0 \\
0 & 0 & t_0 & 0 & 0 & 0 & 0 & t_0 & 0 & 0 & 0 & t_0 & 0 & 0 & 0 & 0 & 0 & 0 & t_3 + t_4 + t_5 \\
0 & 0 & 0 & t_0 & 0 & 0 & t_0 & 0 & t_0 & 0 & 0 & 0 & 0 & 0 & 0 & 0 & 0 & 0 & t_3 \\
0 & 0 & 0 & 0 & t_0 & 0 & 0 & t_0 & 0 & t_0 & 0 & 0 & 0 & 0 & 0 & 0 & 0 & 0 & 0 \\
0 & 0 & 0 & 0 & 0 & t_0 & 0 & 0 & t_0 & 0 & t_0 & 0 & 0 & 0 & 0 & 0 & 0 & 0 & t_4 \\
t_0 & 0 & 0 & 0 & 0 & 0 & 0 & 0 & 0 & t_0 & 0 & t_0 & 0 & 0 & 0 & 0 & 0 & 0 & 0 \\
0 & t_0 & 0 & 0 & 0 & 0 & t_0 & 0 & 0 & 0 & t_0 & 0 & 0 & 0 & 0 & 0 & 0 & 0 & t_5 \\
0 & 0 & t_0 & t_0 & 0 & 0 & 0 & 0 & 0 & 0 & 0 & 0 & 0 & t_0 & 0 & 0 & 0 & t_0 & t_1 \\
0 & 0 & 0 & t_0 & t_0 & 0 & 0 & 0 & 0 & 0 & 0 & 0 & t_0 & 0 & t_0 & 0 & 0 & 0 & t_2 + t_4 + t_5 \\
0 & 0 & 0 & 0 & t_0 & t_0 & 0 & 0 & 0 & 0 & 0 & 0 & 0 & t_0 & 0 & t_0 & 0 & 0 & t_1 + t_3 \\
t_0 & 0 & 0 & 0 & 0 & t_0 & 0 & 0 & 0 & 0 & 0 & 0 & 0 & t_0 & 0 & t_0 & 0 & t_0 & t_2 + t_5 \\
t_0 & t_0 & 0 & 0 & 0 & 0 & 0 & 0 & 0 & 0 & 0 & 0 & 0 & 0 & t_0 & 0 & t_0 & t_1 + t_3 + t_4 \\
0 & t_0 & t_0 & 0 & 0 & 0 & 0 & 0 & 0 & 0 & 0 & 0 & t_0 & 0 & 0 & 0 & t_0 & 0 & t_2 \\
0 & 0 & 0 & 0 & 0 & 0 & t_3 + t_4 + t_5 & t_3 & 0 & t_4 & 0 & t_5 & t_1 & t_2 + t_4 + t_5 & t_1 + t_3 & t_2 + t_5 & t_1 + t_3 + t_4 & t_2 & 0
\end{pmatrix}.$$

(B.6)

The symmetry on the level of the full Hamiltonian $H_L^{(6)}$ is given by

$$
Q^{(6)} = \hat{C}_6 \oplus \overline{Q}^{(6)} =
\begin{pmatrix}
0 & 0 & 0 & 0 & 0 & 1 \\
1 & 0 & 0 & 0 & 0 & 0 \\
0 & 1 & 0 & 0 & 0 & 0 \\
0 & 0 & 1 & 0 & 0 & 0 \\
0 & 0 & 0 & 1 & 0 & 0 \\
0 & 0 & 0 & 0 & 1 & 0
\end{pmatrix}
\tag{B.7}
$$

$$
\oplus
\begin{pmatrix}
\frac{3}{8} & \frac{1}{4} & -\frac{1}{8} & \frac{1}{8} & -\frac{1}{4} & \frac{5}{8} & -\frac{3}{8} & \frac{1}{8} & 0 & -\frac{1}{8} & \frac{3}{8} & 0 & 0 \\
\frac{5}{8} & \frac{3}{8} & \frac{1}{4} & -\frac{1}{8} & \frac{1}{8} & -\frac{1}{4} & 0 & -\frac{3}{8} & \frac{1}{8} & 0 & -\frac{1}{8} & \frac{3}{8} & 0 \\
-\frac{1}{4} & \frac{5}{8} & \frac{3}{8} & \frac{1}{4} & -\frac{1}{8} & \frac{1}{8} & \frac{3}{8} & 0 & -\frac{3}{8} & \frac{1}{8} & 0 & -\frac{1}{8} & 0 \\
\frac{1}{8} & -\frac{1}{4} & \frac{5}{8} & \frac{3}{8} & \frac{1}{4} & -\frac{1}{8} & -\frac{1}{8} & \frac{3}{8} & 0 & -\frac{3}{8} & \frac{1}{8} & 0 & 0 \\
-\frac{1}{8} & \frac{1}{8} & -\frac{1}{4} & \frac{5}{8} & \frac{3}{8} & \frac{1}{4} & \frac{1}{8} & -\frac{1}{8} & \frac{3}{8} & 0 & -\frac{3}{8} & \frac{1}{8} & 0 \\
\frac{1}{4} & -\frac{1}{8} & \frac{1}{8} & -\frac{1}{4} & \frac{5}{8} & \frac{3}{8} & \frac{3}{8} & \frac{1}{8} & -\frac{1}{8} & \frac{3}{8} & 0 & -\frac{3}{8} & 0 \\
0 & -\frac{3}{8} & \frac{1}{8} & 0 & -\frac{1}{8} & \frac{3}{8} & \frac{3}{8} & -\frac{1}{4} & \frac{1}{8} & -\frac{1}{8} & \frac{1}{4} & \frac{3}{8} & 0 \\
\frac{3}{8} & 0 & -\frac{3}{8} & \frac{1}{8} & 0 & -\frac{1}{8} & \frac{5}{8} & \frac{3}{8} & -\frac{1}{4} & \frac{1}{8} & -\frac{1}{8} & \frac{1}{4} & 0 \\
-\frac{1}{8} & \frac{3}{8} & 0 & -\frac{3}{8} & \frac{1}{8} & 0 & \frac{1}{4} & \frac{5}{8} & \frac{3}{8} & -\frac{1}{4} & \frac{1}{8} & -\frac{1}{8} & 0 \\
0 & -\frac{1}{8} & \frac{3}{8} & 0 & -\frac{3}{8} & \frac{1}{8} & -\frac{1}{8} & \frac{1}{4} & \frac{5}{8} & \frac{3}{8} & -\frac{1}{4} & \frac{1}{8} & 0 \\
\frac{1}{8} & 0 & -\frac{1}{8} & \frac{3}{8} & 0 & -\frac{3}{8} & \frac{1}{8} & -\frac{1}{8} & \frac{1}{4} & \frac{5}{8} & \frac{3}{8} & -\frac{1}{4} & 0 \\
-\frac{3}{8} & \frac{1}{8} & 0 & -\frac{1}{8} & \frac{3}{8} & 0 & -\frac{1}{4} & \frac{1}{8} & -\frac{1}{8} & \frac{1}{4} & \frac{5}{8} & \frac{3}{8} & 0 \\
0 & 0 & 0 & 0 & 0 & 0 & 0 & 0 & 0 & 0 & 0 & 0 & 1
\end{pmatrix}.
$$

The reduced parameters that enter Fig. 3(h) and Eq. (56) are of the form

$$
a^{(4)} = \frac{1}{\Delta}\sum_{j=0}^{9}\alpha^{(j)}E^j, \qquad
v_i^{(4)} = \frac{1}{\Delta}\sum_{j=0}^{9}v_i^{(j)}E^j, \qquad
\Delta = \sum_{j=0}^{9}\delta^{(j)}E^j.
\tag{B.8}
$$

The expressions for $\alpha^{(j)}$, $v_i^{(j)}$, and $\delta^{(j)}$ are lengthy, but easily obtainable; they are not given here.

References

[1] A. Altland and M. R. Zirnbauer, *Nonstandard symmetry classes in mesoscopic normal-superconducting hybrid structures*, Phys. Rev. B **55**, 1142 (1997), doi:10.1103/PhysRevB.55.1142.

[2] S. Ryu, A. P. Schnyder, A. Furusaki and A. W. W. Ludwig, *Topological insulators and superconductors: Tenfold way and dimensional hierarchy*, New J. Phys. **12**, 065010 (2010), doi:10.1088/1367-2630/12/6/065010.

[3] R. Roy and F. Harper, *Periodic table for Floquet topological insulators*, Phys. Rev. B **96**, 155118 (2017), doi:10.1103/PhysRevB.96.155118.

[4] J. Li, R.-L. Chu, J. K. Jain and S.-Q. Shen, *Topological Anderson insulator*, Phys. Rev. Lett. **102**, 136806 (2009), doi:10.1103/PhysRevLett.102.136806.

[5] K. Kawabata, K. Shiozaki, M. Ueda and M. Sato, *Symmetry and topology in non-Hermitian physics*, Phys. Rev. X **9**, 041015 (2019), doi:10.1103/PhysRevX.9.041015.

[6] L. Fu, *Topological crystalline insulators*, Phys. Rev. Lett. **106**, 106802 (2011), doi:10.1103/PhysRevLett.106.106802.

[7] C. Fang and L. Fu, *New classes of three-dimensional topological crystalline insulators: Nonsymmorphic and magnetic*, Phys. Rev. B **91**, 161105 (2015), doi:10.1103/PhysRevB.91.161105.

[8] R.-J. Slager, A. Mesaros, V. Juričić and J. Zaanen, *The space group classification of topological band-insulators*, Nat. Phys. **9**, 98 (2012), doi:10.1038/nphys2513.

[9] C. Zhang, Z. Y. Chen, Z. Zhang and Y. X. Zhao, *General theory of momentum-space nonsymmorphic symmetry*, Phys. Rev. Lett. **130**, 256601 (2023), doi:10.1103/PhysRevLett.130.256601.

[10] W. A. Benalcazar, B. A. Bernevig and T. L. Hughes, *Electric multipole moments, topological multipole moment pumping, and chiral hinge states in crystalline insulators*, Phys. Rev. B **96**, 245115 (2017), doi:10.1103/PhysRevB.96.245115.

[11] D. Vanderbilt and R. D. King-Smith, *Electric polarization as a bulk quantity and its relation to surface charge*, Phys. Rev. B **48**, 4442 (1993), doi:10.1103/PhysRevB.48.4442.

[12] R. D. King-Smith and D. Vanderbilt, *Theory of polarization of crystalline solids*, Phys. Rev. B **47**, 1651 (1993), doi:10.1103/PhysRevB.47.1651.

[13] G. van Miert and C. Ortix, *Higher-order topological insulators protected by inversion and rotoinversion symmetries*, Phys. Rev. B **98**, 081110 (2018), doi:10.1103/PhysRevB.98.081110.

[14] W. A. Benalcazar, T. Li and T. L. Hughes, *Quantization of fractional corner charge in C_n-symmetric higher-order topological crystalline insulators*, Phys. Rev. B **99**, 245151 (2019), doi:10.1103/PhysRevB.99.245151.

[15] D. Smith and B. Webb, *Hidden symmetries in real and theoretical networks*, Phys. A: Stat. Mech. Appl. **514**, 855 (2019), doi:10.1016/j.physa.2018.09.131.

[16] M. Röntgen, *Graph-theoretical analysis of local and latent symmetries in physical systems*, PhD thesis, Universität Hamburg, Hamburg, Germany (2022).

[17] L. Bunimovich and B. Webb, *Isospectral transformations: A new approach to analyzing multidimensional systems and networks*, Springer, New York, USA, ISBN 9781493913756 (2014), doi:10.1007/978-1-4939-1375-6.

[18] M. Kempton, J. Sinkovic, D. Smith and B. Webb, *Characterizing cospectral vertices via isospectral reduction*, Linear Algebra Appl. **594**, 226 (2020), doi:10.1016/j.laa.2020.02.020.

[19] C. V. Morfonios, M. Röntgen, M. Pyzh and P. Schmelcher, *Flat bands by latent symmetry*, Phys. Rev. B **104**, 035105 (2021), doi:10.1103/PhysRevB.104.035105.

[20] M. Röntgen, M. Pyzh, C. V. Morfonios, N. E. Palaiodimopoulos, F. K. Diakonos and P. Schmelcher, *Latent symmetry induced degeneracies*, Phys. Rev. Lett. **126**, 180601 (2021), doi:10.1103/PhysRevLett.126.180601.

[21] M. Röntgen, X. Chen, W. Gao, M. Pyzh, P. Schmelcher, V. Pagneux, V. Achilleos and A. Coutant, *Latent Su-Schrieffer-Heeger models*, (arXiv preprint) doi:10.48550/arXiv.2310.07619.

[22] L. Eek, A. Moustaj, M. Röntgen, V. Pagneux, V. Achilleos and C. M. Smith, *Emergent non-Hermitian models*, Phys. Rev. B **109**, 045122 (2024), doi:10.1103/PhysRevB.109.045122.

[23] M. Röntgen, M. Pyzh, C. V. Morfonios and P. Schmelcher, *On symmetries of a matrix and its isospectral reduction*, (arXiv preprint) doi:10.48550/arXiv.2105.12579.

[24] J.-M. Hou and W. Chen, *Hidden antiunitary symmetry behind "accidental" degeneracy and its protection of degeneracy*, Front. Phys. **13**, 130301 (2017), doi:10.1007/s11467-017-0712-8.

[25] H. McIntosh, *Symmetry and degeneracy*, in *Group theory and its applications*, Academic Press, New York, USA, ISBN 9780124551527 (1971), doi:10.1016/B978-0-12-455152-7.50008-2.

[26] C. Fang, M. J. Gilbert and B. A. Bernevig, *Bulk topological invariants in non-interacting point group symmetric insulators*, Phys. Rev. B **86**, 115112 (2012), doi:10.1103/PhysRevB.86.115112.

[27] M. Röntgen, N. E. Palaiodimopoulos, C. V. Morfonios, I. Brouzos, M. Pyzh, F. K. Diakonos and P. Schmelcher, *Designing pretty good state transfer via isospectral reductions*, Phys. Rev. A **101**, 042304 (2020), doi:10.1103/PhysRevA.101.042304.

[28] C. D. Godsil and B. D. McKay, *Constructing cospectral graphs*, Aeq. Math. **25**, 257 (1982), doi:10.1007/BF02189621.

[29] A. J. Schwenk, *Almost all trees are cospectral*, in *New directions in the theory of graphs*, Academic Press, New York, USA, ISBN 9780123242556 (1973).

[30] S. Liu, W. Gao, Q. Zhang, S. Ma, L. Zhang, C. Liu, Y. J. Xiang, T. J. Cui and S. Zhang, *Topologically protected edge state in two-dimensional Su-Schrieffer-Heeger circuit*, Research 8609875 (2019), doi:10.34133/2019/8609875.

[31] A. Coutant, V. Achilleos, O. Richoux, G. Theocharis and V. Pagneux, *Topological two-dimensional Su-Schrieffer-Heeger analog acoustic networks: Total reflection at corners and corner induced modes*, J. Appl. Phys. **129**, 125108 (2021), doi:10.1063/5.0042406.

[32] F. Liu, *Analytic solution of n-dimensional Su-Schrieffer-Heeger model*, Phys. Rev. B **108**, 24514 (2023), doi:10.1103/PhysRevB.108.245140.

[33] C. J. Dai, X. H. Yan, Y. Xiao and Y. D. Guo, *Electronic and transport properties of T-graphene nanoribbon: Symmetry-dependent multiple Dirac points, negative differential resistance and linear current-bias characteristics*, Europhys. Lett. **107**, 37004 (2014), doi:10.1209/0295-5075/107/37004.

[34] L. H. C. M. Nunes and C. M. Smith, *Flat-band superconductivity for tight-binding electrons on a square-octagon lattice*, Phys. Rev. B **101**, 224514 (2020), doi:10.1103/PhysRevB.101.224514.

[35] L. Yan, D. Zhang, X.-J. Wang and J.-Y. Yan, *Intrinsic topological metal state in T-graphene*, New J. Phys. **25**, 043020 (2023), doi:10.1088/1367-2630/acccd7.

[36] S. N. Kempkes, M. R. Slot, J. J. van den Broeke, P. Capiod, W. A. Benalcazar, D. Vanmaekelbergh, D. Bercioux, I. Swart and C. M. Smith, *Robust zero-energy modes in an electronic higher-order topological insulator*, Nat. Mater. **18**, 1292 (2019), doi:10.1038/s41563-019-0483-4.

[37] G. van Miert and C. Ortix, *On the topological immunity of corner states in two-dimensional crystalline insulators*, npj Quantum Mater. **5**, 63 (2020), doi:10.1038/s41535-020-00265-7.

[38] M. A. J. Herrera, S. N. Kempkes, M. Blanco de Paz, A. García-Etxarri, I. Swart, C. M. Smith and D. Bercioux, *Corner modes of the breathing kagome lattice: Origin and robustness*, Phys. Rev. B **105**, 085411 (2022), doi:10.1103/PhysRevB.105.085411.

[39] L.-H. Wu and X. Hu, *Scheme for achieving a topological photonic crystal by using dielectric material*, Phys. Rev. Lett. **114**, 223901 (2015), doi:10.1103/PhysRevLett.114.223901.

[40] S. E. Freeney, J. J. van den Broeke, A. J. J. Harsveld van der Veen, I. Swart and C. M. Smith, *Edge-dependent topology in Kekulé lattices*, Phys. Rev. Lett. **124**, 236404 (2020), doi:10.1103/PhysRevLett.124.236404.

[41] A. Moustaj, J. P. J. Krebbekx and C. M. Smith, *Anomalous polarization in one-dimensional aperiodic insulators*, Condens. Matter **10**, 3 (2025), doi:10.3390/condmat10010003.

[42] R. Canyellas et al., *Topological edge and corner states in bismuth fractal nanostructures*, Nat. Phys. **20**, 1421 (2024), doi:10.1038/s41567-024-02551-8.

[43] M. Ezawa, *Higher-order topological insulators and semimetals on the breathing kagome and pyrochlore lattices*, Phys. Rev. Lett. **120**, 026801 (2018), doi:10.1103/PhysRevLett.120.026801.